

## A Search for High Energy Neutrinos from Active Galactic Nuclei

J. W. Bolesta, P. W. Gorham <sup>1</sup>, J. G. Learned, S. Matsuno, V. J. Stenger,  
S. Kondo, D. J. O'Connor, V. Peterson  
University of Hawaii, USA

Y. Ohashi, A. Okada  
Institute of Cosmic Ray Research, University of Tokyo, Japan

T. Hayashino, T. Matsumoto <sup>2</sup>, A. Yamaguchi  
Tohoku University, Japan

S. Uehara  
National Laboratory for High Energy Physics (KEK), Japan

P. Koske  
University of Kiel, Germany

J. Hauptman, K. Mauritz  
Iowa State University, USA

P. K. F. Grieder, P. Minkowski  
University of Bern, Switzerland

S. T. Dye <sup>3</sup>  
Boston University, USA

H. Bradner  
Scripps Institute of Oceanography, USA

M. Webster, J. Clem <sup>4</sup>  
Vanderbilt University, USA

R. J. Wilkes, K. K. Young, J. George  
University of Washington, USA

U. Camerini, R. March, T. Narita

---

<sup>1</sup>Presently at Jet Propulsion Laboratory, USA

<sup>2</sup>Presently at Sakuyo Junior College, Japan

<sup>3</sup>Presently at Hawaii Pacific University, USA

<sup>4</sup>presently at Bartol Research Institute, USA

University of Wisconsin, USA

P.C. Bosetti, C. Wiebusch  
Aachen University, Germany

## ABSTRACT

We report the results of a search for neutrino-induced particle cascades using a deep ocean water Čerenkov detector. Previous results using this instrument have demonstrated its effectiveness for tracking cosmic-ray muons in depths up to 4.2 km. Here we analyze the same data to search for the possible signature of ultra-high energy neutrinos. Potentially detectable fluxes of such neutrinos are predicted to come from active galactic nuclei according to some models. The effective mass of the detector, a string of seven 40 cm photomultipliers at 5.2 m spacing, is found through simulation analysis to be surprisingly large: greater than  $10^6$  tons of water at incident neutrino energies of  $10^6$  GeV. We find no evidence for neutrino-induced cascades in  $\sim 20$  hrs of operation. Although the limit implied by this observation is the strongest yet for predictions of active galactic nuclei (AGN) neutrinos at energies above 100 TeV, perhaps the more intriguing result is that the power of these techniques can be exploited to test these AGN models in a relatively short time.

*Subject headings:* Active galactic nuclei: neutrinos : cosmic rays

## 1. Introduction

### 1.1. Neutrino Emission from AGNs

Suggestions that hadronic processes may play an important role in the dynamics of Active Galactic Nuclei (AGN) began almost two decades ago (Berezinsky 1977), yet there is still no direct observation that compels us to believe any of the numerous models that have been proposed since that time. Observations of TeV photons from Markarian 421 (Buckley et al. 1996; Gaidos et al 1996) are probably consistent with either hadronic or electromagnetic processes; TeV energies are still within the regime where either can play a dominant role. Perhaps the best indirect evidence for hadronic processes comes from the highest energy cosmic rays. Yet these may still be produced by Fermi processes in nearby galaxies without the necessity of a hadronic plasma near the central engine of an AGN.

The importance of identifying whether or not there is significant shock acceleration of protons near the center of AGNs is simply this: until we gain more detailed information about it, we cannot yet say that we understand how the engine works, at least in terms of the phenomenology of the

transfer of energy to the surrounding galaxy (cf. Gaisser, Halzen, and Stanev 1995; von Montigny et al. 1996). If the central engine is cooled primarily through photon-electron interactions, then momentum transfer proceeds in an entirely different way than if the dominant components are hadrons. In the latter case, neutral particles other than photons begin to play a major role in the momentum and energy transfer through the agency of neutrinos and neutrons, both of which can easily escape the high particle and field density of the central engine environment.

Consequently, the observation of high-energy neutrinos from Earth is of critical importance to our understanding of the most powerful objects in the universe. In this paper we report results which mark an important step toward developing the tools which will begin solving this riddle.

## 1.2. AGN Neutrino Detection Method

The idea behind our measurement of the neutrino flux is, in essence, extensive air shower (EAS) detection, except in the ocean. Due to the optical properties of the deep ocean and the fact that water is  $\sim 10^3$  more dense than the atmosphere, detector livetimes can accrue at a rate of  $\sim 100$  kiloton-years (kty) *per day*, for neutrinos of energy  $\sim 100$  PeV.

We have re-analyzed data that was recorded in 1987 by a prototype of the planned Deep Underwater Muon and Neutrino Detector (DUMAND), a  $\sim 30$  m-long linear array of seven 40 cm photomultiplier modules. Our motivation for this was the realization that the deep ocean has one property that appears to be unmatched in any other presently accessible medium that is used for similar water or ice Čerenkov detectors: a remarkably long scattering length in the deepest waters. This has been documented by oceanographers (cf. Jerlov 1976; Shifrin 1983) and in practice allows one to observe a sufficiently bright source at distances out to many hundreds of meters before the effects of diffusive scattering of the light become significant. The volume of water that is potentially accessible to even a relatively small detector can begin to approach a cubic km for events which produce sufficient light to penetrate to optical depths of six or more.

This is likely to be satisfied by neutrino interactions at high energies. If the energy of the incident neutrino is above 100 TeV or so, the interaction will produce an intense hadronic or electromagnetic cascade of particles that will rapidly develop and decay in the water near the point of the initial neutrino interaction. The length scale for this is of order 10 m in water, and the number of charged particles produced will be  $\geq 10^5$ , scaling up with energy. These cascades then produce an extremely bright flash of Čerenkov emission containing  $\geq 10^{11}$  photons in the visible and near UV. This flash arrives at the detector as a spherical, or at great distances, a plane-wave of risetime  $\ll 100$  ns. Such events are unique in the deep ocean; there is no known background at such short durations except that which may be produced from cosmic rays.

A search for these type of events with what is designed to be a muon-tracking instrument represents a response to the predictions of most of the AGN neutrino models, that the peak detectability ratio for neutrino observations may be attained at much higher energies (PeV rather

than TeV) than initially thought (cf. Stecker and Salomon 1996; Gaisser et al. 1995). The advantage of searching for cascades rather than muons comes from the fact that, in a cascade, all of the available Čerenkov emission is produced locally at the shower, rather than quasi-continuously along a muon track which may extend many kilometers. In the latter case most of the emission goes unobserved, and even that which is observed tends to only be detected with a small number of detector modules. In contrast a PeV cascade has a good probability of illuminating the entire array at light levels producing multiple photoelectron events in many, if not all, of the detector modules. And because such events are so unlike the typical few-hundred GeV cosmic-ray muon event, one may also look for them above the horizon, which thus extends the useful solid angle for the detector.

Because this experiment only yielded about 20 hrs usable livetime for our search, we find that the sensitivity is not adequate to constrain present models for AGN neutrino emission except in the broadest sense. Yet we can report that even this short observation is sufficient to produce a limit at energies above 1 PeV that is better than any other published limit. This clearly demonstrates the viability and power of an ocean-based high energy neutrino detector.

### 1.3. Outline of the Paper

In section two below, we briefly summarize the experiment. Section three deals with the optical properties of the ocean. We begin by listing the standard types of oceanographic measurements that constitute our knowledge of the experimental site. We then proceed with a short review of ocean optics, using the conventions of physical oceanography, in order to elucidate how these measurements are synthesized into a cohesive model of light transport in the ocean. Next, we present our determination of the optical properties of the site, and finish the section with a discussion of the implications for neutrino detection. In section four, we present in some detail the simulations involved in our analysis. These include event generation, signals and backgrounds, photon propagation, detector response, as well as a comparison with the original analysis. We end the section with our calculation of the effective mass of the experiment for neutrino detection. Section five presents our search of the SPS data for AGN neutrinos. Given the null results of two, independent tests for such a signal, we calculate our upper limit of the diffuse neutrino flux from AGNs and compare it to other limits. In section six, we discuss some of the results of our analysis, and their implications for other neutrino detectors (either in operation or under construction). Section seven ends the paper with some concluding remarks.

## 2. Description of the Experiment

The details of the experiment are reported in Babson et al. (1990). We summarize these briefly here. Observations were made during November 1987 using the RV Kaimalino, at a site

$\sim 35$  km west of Keahole Point, Hawaii Island, near 156.325 W and 19.375 N. Observations were made over depths ranging from 2–4 km for a duration of  $\sim 30$  hrs. Here we use only the data deeper than 3 km because of uncertainty in the sensitivity for the shallower depths.

The detector, called the Short Prototype String (SPS), consisted of a string of seven Hamamatsu 37 cm diameter hemispherical photomultiplier tubes (PMTs) contained in 40 cm diameter deep ocean pyrex instrument housings spaced at equidistant intervals of 5.18 m. Local PMT pulse shaping was performed within the housing. The entire PMT+electronics+housing system is designated an optical module (OM). The OMs are described in more detail in Matsuno et al. (1989).

Digitizing, data multiplexing, and power control was performed at the base of the string by the string bottom controller (SBC), to which each OM transmitted its individual pulses over a multi-mode fiber link after analog pulse shaping. Once digitized, the data was multiplexed and transmitted up a single-mode fiber to the ship, where coincidence logic was used to distinguish possible muon Čerenkov events. The time of arrival at each OM as well as the approximate logarithm of the detected charge (photoelectrons or  $pe$ ) were recorded for later analysis.

The Hamamatsu PMTs are not uniformly sensitive in polar angle. Thus the OMs were arranged to have their maximum sensitivity toward the zenith, to afford the best sensitivity to the predominantly downgoing muons. Their sensitivity in the backward hemisphere averages only about 25% of that in the forward hemisphere. In addition, the trigger system was optimized for downgoing muon events. The combination of both of these effects reduces the efficiency of the detector for events in the lower hemisphere (such as upcoming muons from neutrinos) and the sensitivity falls off rapidly beyond  $20 - 30^\circ$  below the horizon.

Observations were made primarily with the intent of measuring the muon depth-intensity relation over the range of 2-4  $kmwe$  (km of water equivalent). To ensure that the effective area of the detector to muons could be estimated for each depth, a pair of laser calibration modules (CMs) were used: two 337 nm lasers pulsed scintillator balls that were 2 m off the string axis and 7.8 m below its top and above its bottom. Because of stability problems with the bottom CM, we have used only the pulses from the top CM in these analyses. The laser pulse was delivered to the scintillator through an optical fiber bundle isolated in a light-tight tube. The scintillator was fast enough in its response and decay so that it was much less than the OM PMT response, and its effective wavelength was 430 nm.

### 3. Optical Properties of Site

Since much of the power of this technique depends on the optical properties of the detection medium, this section will describe the analysis of data relating to these parameters in some detail. Our knowledge of the site optical properties at the depths of interest come from three sources:

- (a) Direct measurement using the laser calibration system. We present reanalysis of these data here, finding results consistent with those of Clem (1990).
- (b) Beam transmissometer measurements of Zaneveld (1980), from the surface down to 4.5 km depth, at a variety of wavelengths.
- (c) Measurements of microscopic particle concentration, also by Zaneveld (1978; 1980).

To understand how these measurements can be synthesized into the parameters necessary for estimating our experimental sensitivity, we briefly review the standard models for ocean optical properties, using the conventions of physical oceanography.

### 3.1. Attenuation

The global optical properties of water may be characterized in terms of the beam attenuation coefficient  $c_w(\lambda)$  for wavelength  $\lambda$ , or alternately the diffuse attenuation coefficient  $K_w(\lambda)$ . A beam transmissometer typically measures something close to  $c_w(\lambda)$ , which may be regarded as the inverse mean-free-path of the light to either absorption or scattering of any sort. In practice, since the instruments used to measure  $c_w(\lambda)$  have a small, finite acceptance angle,  $c_w(\lambda)$  actually measures the inverse mean-free-path for absorption or scattering above some small angle, typically  $\sim 1^\circ$ .

In contrast the diffuse attenuation coefficient is defined as:

$$K_w(\lambda) \equiv \frac{\ln[I(z_1)] - \ln[I(z_2)]}{z_2 - z_1} \quad (1)$$

where  $I(z)$  is the irradiance at depth (or distance)  $z$ . This parameter is what is estimated using Secchi disk measurements with solar irradiance, and it allows in principle for multiple scattering, as long as the general shape of the disk is still recognizable. In recent years, more sophisticated radiometers have been used for  $K_w$  measurements (cf. Smith and Baker 1981), but  $K_w$  is still almost universally measured for waters within a few attenuation lengths of the surface, using solar irradiation. Estimates of diffuse attenuation in deep waters, which are the clearest waters in the ocean, must typically be extrapolated from beam attenuation measurements.

For our purposes, the detector is a hemispherical photomultiplier with a sensitivity that is useful over most of the  $4\pi$  solid angle surrounding it. However, for an event to be detected the time coherence of the wavefront must be roughly preserved over the integration time for the charge at the anode of the PMT, a few hundred nanoseconds. Thus single or multiple scattering that smears out the time structure too much will reduce the sensitivity, and this effect ultimately limits the distance out to which the detector can see. For this reason neither  $c_w(\lambda)$  or  $K_w(\lambda)$  are the exact parameters of interest, though they appear to bound the value that is most relevant. In

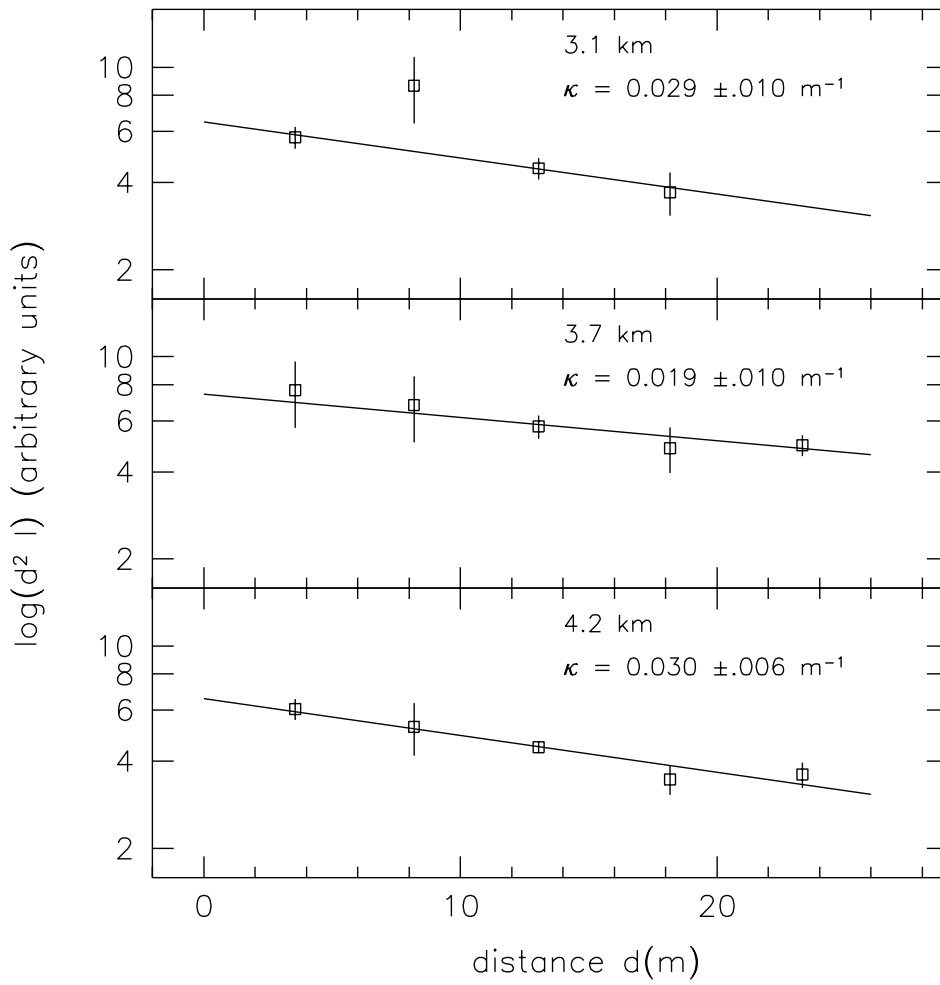


Fig. 1.— The effective diffuse attenuation coefficient  $\kappa_w$  at 430 nm at the experiment site as measured from the laser calibration system at the three depths of data used here.

what follows we denote the effective diffuse attenuation coefficient relevant to our optical modules as  $\kappa_w(\lambda)$ .

Figure 1 plots results on the beam attenuation coefficient as determined from the laser calibration data at three depths in the range of data analyzed here: 3.1, 3.7, and 4.2 km. All of the coefficients determined are consistent with each other, and we have thus combined them into a single estimate:

$$\kappa_w(430 \text{ nm}) = 0.027 \pm 0.0054 \text{ m}^{-1} \quad (2)$$

over the range 3-4.2 km at the experiment site.

### 3.2. Scattering

Light scattering in the ocean has been well-studied and there are numerous compilations of data (cf. Jerlov 1976; Shifrin 1983). The measurements usually determine the angular scattering coefficient  $\beta(\theta, \lambda)$  for polar angle  $\theta$  and wavelength  $\lambda$ , with units of  $\text{m}^{-1} \text{sr}^{-1}$ . There are two main contributions to the scattering function  $\beta$ : scattering from particulate matter ( $\beta_p$ ) and molecular scattering ( $\beta_m$ ), also commonly referred to as Rayleigh scattering.  $\beta_p$  is strongly forward-peaked and only a weak function of  $\lambda$ , while  $\beta_m$  has the familiar  $(1 + \cos^2(\theta))$  dependence and is a strong function of wavelength, with scattering increasing in magnitude as  $\lambda^{-4.2}$  (Shifrin 1983; the deviation from the expected  $\lambda^{-4}$  comes from the correction for the change in index of refraction with wavelength). In addition to the wavelength dependence, in the ocean  $\beta_m$  also has a depth dependence, both from pressure and temperature effects; at greater depths the scattering coefficient decreases. The fractional decrease amounts to  $\sim 12\%$  at the depths of our observations.

It has been found empirically (Petzoldt 1972) that the particle scattering function  $\beta_p$  has a behavior that scales closely to the concentration of particulate matter in the water, and retains its global angular dependence over a wide range of such concentrations. Since the molecular scattering function  $\beta_m$  is well-known for seawater, the total scattering function can be estimated reliably once the particle concentration is known, assuming there are no anomalous species of particle type among those present. Such methods have been used by Shifrin (1983) and others to estimate  $\beta$  and have been found to be remarkably accurate.

Since to date we have no direct measurements of the scattering function at the site of our observations, we have used these indirect techniques to estimate  $\beta$  based on the measurements of particulate concentration by Zaneveld (1980).

In Figure 2 we plot our estimate of  $\kappa_w(\lambda)$  along with the results from Zaneveld (1980) for  $c_w(\lambda)$ . Our estimate of  $\kappa_w(\lambda)$  obtained by first fitting a model for the deep ocean beam attenuation function to the measured data of Zaneveld (1980) for our site. This model beam attenuation function is then adjusted with numerically integrated estimates of the scattering corrections, based on a Petzoldt scattering function that fits the measurements of Zaneveld (1980) of the site's

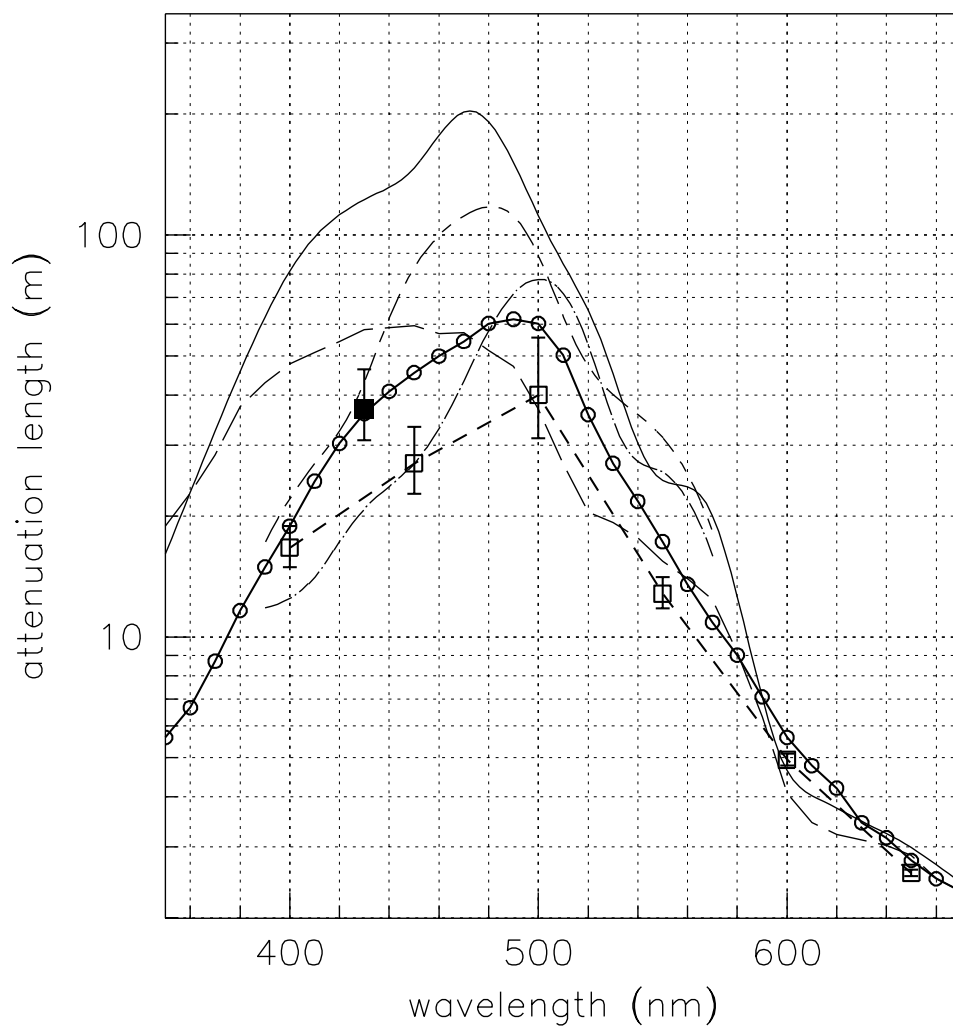


Fig. 2.— The effective diffuse spectral attenuation length (solid line with circles) used here, estimated from the beam attenuation length (open squares joined with short-dashed lines) determined by Zaneveld (1980). The filled square is the combined value of the measurements of the laser calibration system for this work, which provides an estimate of the effective diffuse attenuation length at the wavelength plotted. The upper curve (solid line) is the measurement of James and Birge (1938) for the absorption of pure water; the next highest and third highest (short-long dash; dot-dash) curves are measurements of Shifrin (1983) of absorption in the Tonga Trench (10 km depth) and N. Pacific surface water (85 m depth). The long-dash curve is that of Smith and Baker (1981) for their estimate of the diffuse attenuation coefficient for the clearest ocean surface waters.

particle concentration. A consistency check on the result is provided by our direct measurement of  $\kappa_w(430 \text{ nm})$  (filled square in Fig. 2), which is consistent with the numerical result.

Since the beam attenuation function assumes that any scattering removes the light from possible detection, we adjust this by integrating  $\beta(\theta, \lambda)$  over the full acceptance angle of the OM to determine how much light will single-scatter back into the OM. The continuity equation requires that the light scattered out of the beam equal that scattered back in; however, the beam attenuation coefficient accounts for light scattering out without allowing light to scatter back in. A final check in the process is to require that the time delay of any scattered photons is small compared to the response time of the OM. This prescription is found to be accurate out to  $\sim 100 \text{ m}$ , approximately one scattering mean-free-path for our site. We will discuss the extension to larger distances in the sections that follow.

In Figure 2 we have also plotted a number of attenuation and absorption functions along with our data and  $\kappa_w$  estimate for comparison. The curves included are not a complete set, but provide some indication of the variance in measurements. The highest curve belongs to the measurements of absorption of pure water by James and Birge (1938; solid line), using a transmissometer with a silver-lined tube. The absorption is determined by correcting the transmissometer measurements for the known molecular scattering effects. This result has been criticized in the intervening period (cf. Smith and Tyler 1976 for a summary), but is supported by results of Shifrin (1983). The second highest curve is an absorption measurement near the bottom of the Tonga Trench (long-short dash), and the third highest is absorption from North Pacific surface water at 85 m depth (dot-long dash) (Shifrin 1983). The long-dash curve is the estimate of Smith and Baker (1981) of the diffuse attenuation coefficient for the clearest ocean surface waters, made by combining various measurements of their own and other authors’.

The variation of the measurements plotted in Figure 2 illustrates the physical processes that determine the shape of these curves: in the blue and ultraviolet, molecular scattering increases as  $\sim \lambda^{-4}$ , and particle scattering is most efficient; thus the higher particle concentrations of surface waters lead to higher losses, but diffuse measurements are less affected. In the red, absorption by particles and dissolved substances is more important, as well as molecular absorption of water. These are weaker functions of concentration than the scattering, however, and the resulting curves are thus less widely varying than in the blue.

The scattering mean free path  $L_\beta$  implied by these measurements, calculated from the integral of the fitted model for  $\beta$  over  $\theta$  is  $L_\beta = 105 \pm 15 \text{ m}$  at 480 nm. In the following section we discuss in more detail the way scattering is parameterized in the ocean.

### 3.2.1. *Effective Scattering Length*

Because of the strong forward peak to  $\beta(\theta)$ , a detector with a wide acceptance angle can receive many scattered photons as well as the direct light. If the mean scattering angle is small

enough, photons may undergo multiple scattering and still be detected within the coincidence time of the detector, as discussed above. Thus the detector will be sensitive to a volume with a radius which extends to some multiple of the scattering length. Measurements of ocean scattering are often parameterized in terms of the mean cosine of the scattering,  $\langle \cos \theta \rangle$ , which indicates the magnitude of the forward component of the scattering in terms of solid angle (Shifrin 1983). One may then define an effective scattering length:

$$L_{eff} \equiv \frac{L_{\beta}}{[1 - \langle \cos \theta \rangle]} \quad (3)$$

where  $\langle \cos \theta \rangle$  is the mean of the cosine of the scattering angle.

The physical interpretation of  $L_{eff}$  is that it is the distance at which  $1 - \frac{1}{e}$  of the photons have been scattered into the backward hemisphere, relative to the original direction. It does not mean that the distribution is isotropic at this point, since  $exp(-L_{eff}/L_{\beta})$  of the original light has undergone no scattering (though possibly absorbed). Rather,  $L_{eff}$  gives a transition distance at which the propagation of the light moves from geometric optics to a diffusion-dominated regime.

For the data reported here we estimate  $\langle \cos \theta \rangle = 0.65$  at 480 nm, which implies  $L_{eff} \sim 300$  m. Not entirely by coincidence, it is approximately equal to  $L_{Rayl}$  the mean free path for Rayleigh scattering, at the 480 nm peak transmission wavelength in the ocean, corrected for pressure and temperature effects at 4 km. The correlation of the two values comes from the fact that as the ratio of particle scattering to Rayleigh scattering decreases in the clear waters of the deep ocean,  $\langle \cos \theta \rangle$  also decreases; and in the case of no particle scattering present,  $\langle \cos \theta \rangle = 0$ , implying from equation 3 above that  $L_{eff} = L_{Rayl}$  in this limit.

The detector’s ability to distinguish the cascade requires only that some of the light survive in a prompt Čerenkov wavefront. At a distance of 300 m at our site,  $\sim 10\%$  of the surviving light has undergone no scattering at all. Thus the rising edge of this wavefront may still be detected even if there is a trail of scattered photons arriving after it. Beyond this distance, there is the question of what the effects of the diffusion-dominance are in detecting and reconstructing cascades at the highest energies. We will proceed to a more quantitative analysis of these effects in the section that follows.

#### 4. The Effective Mass of the SPS

Since the estimate of the effective mass of the detector is ultimately what determines the sensitivity, we discuss in some detail the simulations used in its determination.

## 4.1. Detector Electronics

Given that the more distinguishing characteristics of cascades are their brightness and angular distribution, we will describe some of the potentially more limiting aspects introduced by the detector itself.

### 4.1.1. Triggering

The trigger coincidence window was fixed in time relative to the arrival of the muon events; thus the efficiency for coincidence levels greater than 5-fold began to fall off due to the increased probability that the event would straddle the coincidence window. The trigger had no provision to capture such events. Effects of comparable importance were the angular sensitivity of the OMs, which falls off in the backward hemisphere, and the absence of a set of fiberoptic delay cables to produce a simultaneous arrival of OMs that were hit simultaneously. This latter effect was significant since the trigger electronics were on the bottom; thus the coincidence window was optimized for downgoing muons, and lacked sensitivity for upcoming events.

Because of the short duration of the observations, and the reduced lower-hemisphere sensitivity, no atmospheric neutrino-induced muons were expected in the data (these would be evident as up-coming muons). None were seen in the original data analysis, or in our post-analysis. Thus we did not include any atmospheric neutrino events in our simulation.

### 4.1.2. OM saturation

Since the original purpose of the experiment was to track cosmic ray muons in the ocean in order to demonstrate the technical feasibility of DUMAND, the original calibration of the SPS OMs, Matsuno et al. (1989), did not include high light levels relevant to our search. Only three of the seven OMs were tested only as high as 36  $pe$ . As a result, we did not know *a priori*, how they would respond to appreciably higher light levels. Upon examination of the original results, we observed that the 36  $pe$  data points, of the three OMs that were tested to 36  $pe$ , appeared to be significantly below the pulse width- $pe$  fitted function. This qualitative ‘chi by eye’ was confirmed in the laboratory upon resurrection of one the original SPS OMs. The PMT itself was not examined due to stability concerns, and the fact that they had already been characterized prior to their acceptance. Rather, we fed simulated PMT output pulses via a pulse generator into the OM processing electronics and recorded the output as shown schematically in Figure 3.

In the OMs, the PMT output was amplified and fed into a discriminator that produced a time-over-threshold (TOT) pulse. This TOT pulse drove a circuit that would linearly charge while the pulse was above threshold and linearly discharge when the pulse fell below threshold. The rate of discharge was nine times longer than the rate of charge (which was commensurate with

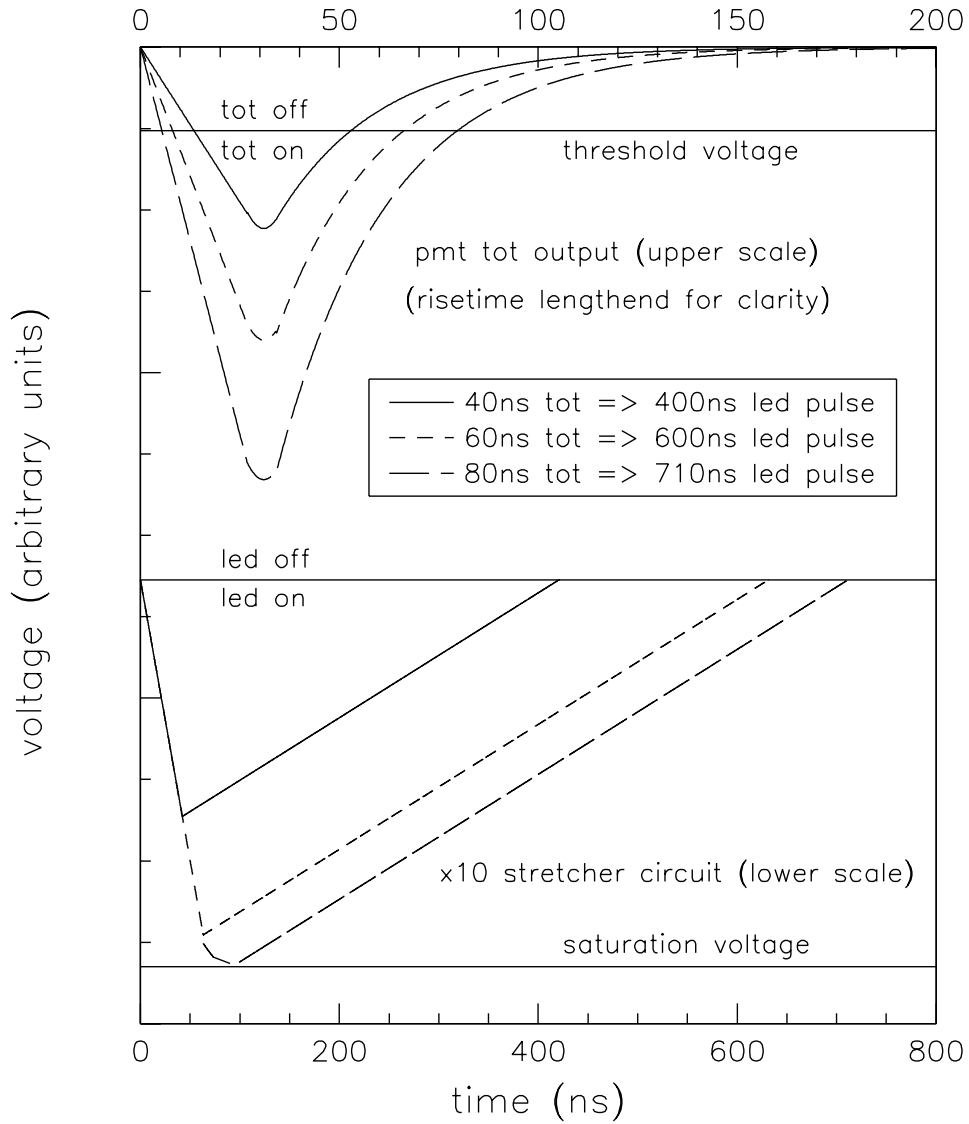


Fig. 3.— The conversion of the TOT pulse to the LED pulse that was digitized in the SBC. The top three curves (upper scale) are PMT TOT pulses of 40,60&80 ns from top to bottom. The bottom three curves (lower scale) are their corresponding output of 400,600&710 ns also from top to bottom.

the risetime). This effectively stretched the PMT TOT pulse by a factor 10. This stretched TOT pulse was converted to an optical pulse by a light emitting diode (LED) which was sent to, and digitized by, the SBC. The x10 stretcher circuit was implemented to improve the resolution given the digitizing clock speed of 200 MHz (5 ns least count). This x10 stretcher circuit would begin to saturate at a PMT TOT of  $\sim 60$  ns, as suspected, and would be in full saturation at a PMT TOT of  $\sim 80$  ns. Once the circuit was in full saturation, the remaining TOT would simply add to the already stretched pulse. At this point, the PMT itself was beginning to saturate and consequently, a single PMT pulse would not rise much above  $\sim 800$  ns.

Figure 4 shows the results of the above considerations as manifested in the Monte Carlo. The graph at the top of Figure 4 is of the original OM pulse width- $pe$  calibration measurement. The dashed line is the function that was fit to the data and used in the original analysis. Note the dubious high- $pe$  data point. The bottom graph shows the output of our Monte Carlo, plotted on top of the original results, after accounting for the limited dynamic range of the SPS OMs. The Monte Carlo pulse widths versus  $pe$  plotted in the bottom graph of Figure 4 are from pure cascades for clarity of comparison; they do not include noise hits, showering muons, data transmission loss etc., though these and all other effects were turned on for the analysis.

We will show in a later section that OM saturation did not affect our results.

## 4.2. Atmospheric Muon Simulation

Muon events were simulated using the known atmospheric muon energy spectrum, based on the parameterization given by Miyake (1973). They are propagated through simulated seawater to depth, and the associated effects of catastrophic energy loss are included, as we discuss below. A complementary description of the details of the atmospheric muon simulation used here are given in Okada (1994).

### 4.2.1. Catastrophic energy loss

As discussed in Babson et al. (1990), the SPS muon data shows evidence for catastrophic energy loss along the muon tracks, primarily through bremsstrahlung, pair-production, or nuclear interactions along the muon track. Since events in which catastrophic energy loss occurs near the detector may produce pulse height or timing distributions which are different than the majority of muons, it is important that these processes be simulated in detail, to understand how they may affect the results.

The mean muon energy at our depths for the array is  $\sim 300$  GeV, implying a surface energy of about 3.7 TeV. At higher energies, the energy loss increases in the intervening water column. Thus a vertical muon which reaches the detector with an energy of  $\sim 1$  TeV, enough to begin to

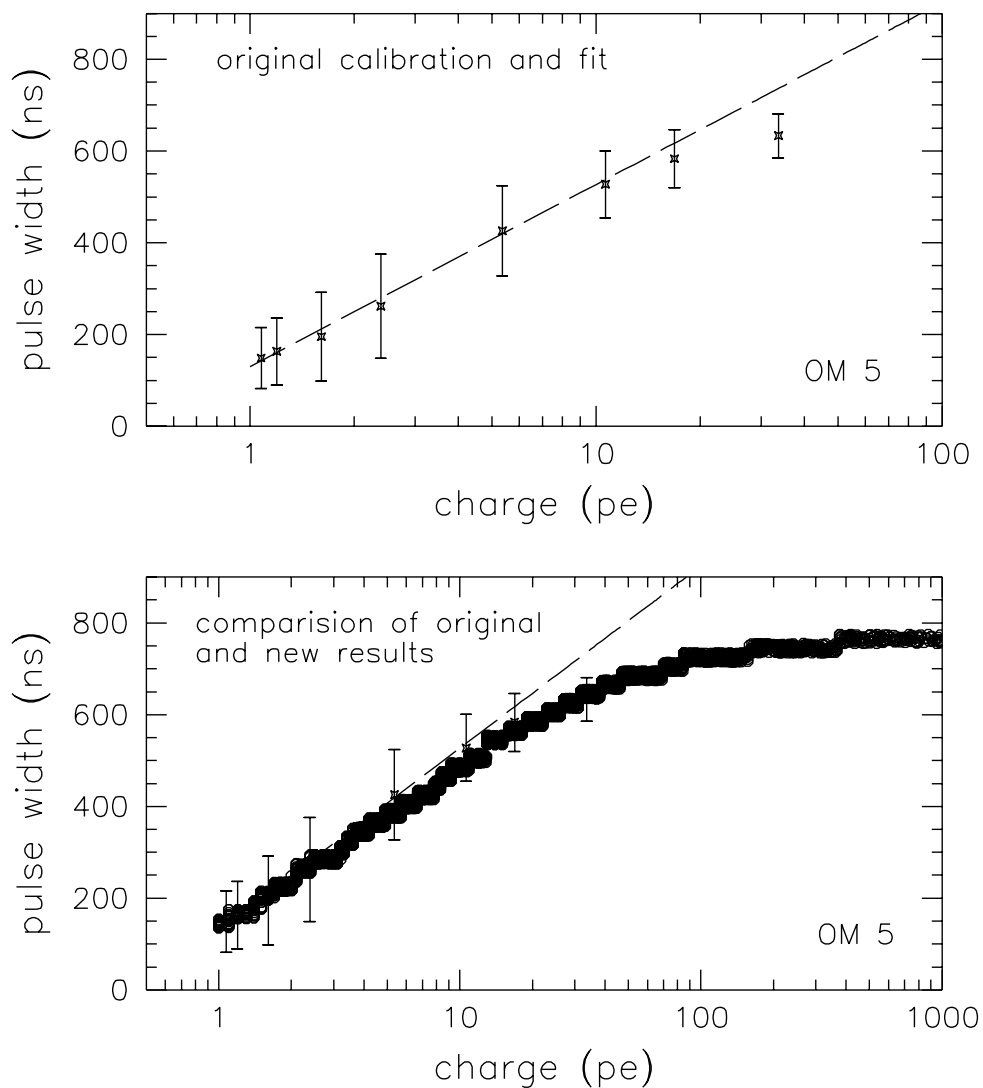


Fig. 4.— Comparison of original calibration results and the output of the Monte Carlo used in this analysis. The top graph shows the OM pulse width to  $pe$  calibration (data points) and the fitted function (dashed line) used for the conversion in the original experiment. The bottom graph shows the output of our Monte Carlo, plotted on top of the original results, after accounting for the limited dynamic range of the SPS OMs.

show detectable effects of catastrophic energy loss, had an initial energy of  $\geq 7 \text{ TeV}$ . Since the integral atmospheric muon spectrum at the surface has a spectral index of  $-2.7$ , and steepens with depth, we estimate that such events comprise only a fraction of order 10% of the data, the majority of which is taken at  $\geq 3.7 \text{ kmwe}$ . Monte Carlo test results which confirm this qualitative estimate are reported in a later section.

#### 4.2.2. Multiple Muons

Multiple muon events comprise a significant fraction of the data at the surface muon threshold energy ( $\sim 2 \text{ TeV}$ ) relevant to our depths. Measurements by the MACRO and EAS-TOP detectors (Hong et al. 1994; Ahlen et al. 1992), acting in coincidence, have shown that the multiple-muon fraction at comparable depths to ours (3100-3500 mwe) was  $\sim 15\%$  near the muon energy threshold. We have therefore simulated our detector response to muon groups with the expected frequency, and also included a fitting parameter so that we could estimate the presence of such events in our muon data sample. We note the results of this fitting in a later section.

### 4.3. Cascade Simulation

The cascade simulation uses the standard high energy physics code GEANT to simulate electromagnetic and hadronic cascades at energies of around 1 TeV, and then estimates the behavior of much higher energy cascades by performing weighted sums of these lower energy cascades. Part of this work is based on that of Levenberg (1992), and extends Levenberg's work to correct for multiple scattering in the particle shower, so that the resulting Čerenkov light distribution is modeled more accurately.

Figure 5 shows three forms for the distribution: the solid line is the Čerenkov angular distribution expected from a cascade initiated by a  $6.3 \times 10^{15} \text{ eV}$  muon neutrino, with all of its energy going into a hadronic cascade; the dashed line is that from an electron neutrino, producing a pure electromagnetic cascade. The dotted line shows the older distribution calculated by Belyaev (1976), without including all of the multiple scattering effects used in our case. These effects tend to smooth the distribution, spreading the light outside the Čerenkov cone. These distributions are also consistent with the results of Wiebusch (1995) who constructed a similar shower model.

The energy 6.3 PeV (1 Pev =  $10^{15} \text{ eV}$ ) is of interest because it is the peak energy of the *Glashow Resonance* (Glashow 1960) for production of W bosons by interaction of an incoming electron antineutrino with an electron in the water. The enhancement of the cross section around this resonance is shown in Figure 6. Since all models of AGN neutrinos predict an electron antineutrino flux which is 1/6 of the total neutrino flux, the enhanced cross section at this resonance may in many cases provide the best opportunity to observe the AGN neutrinos.

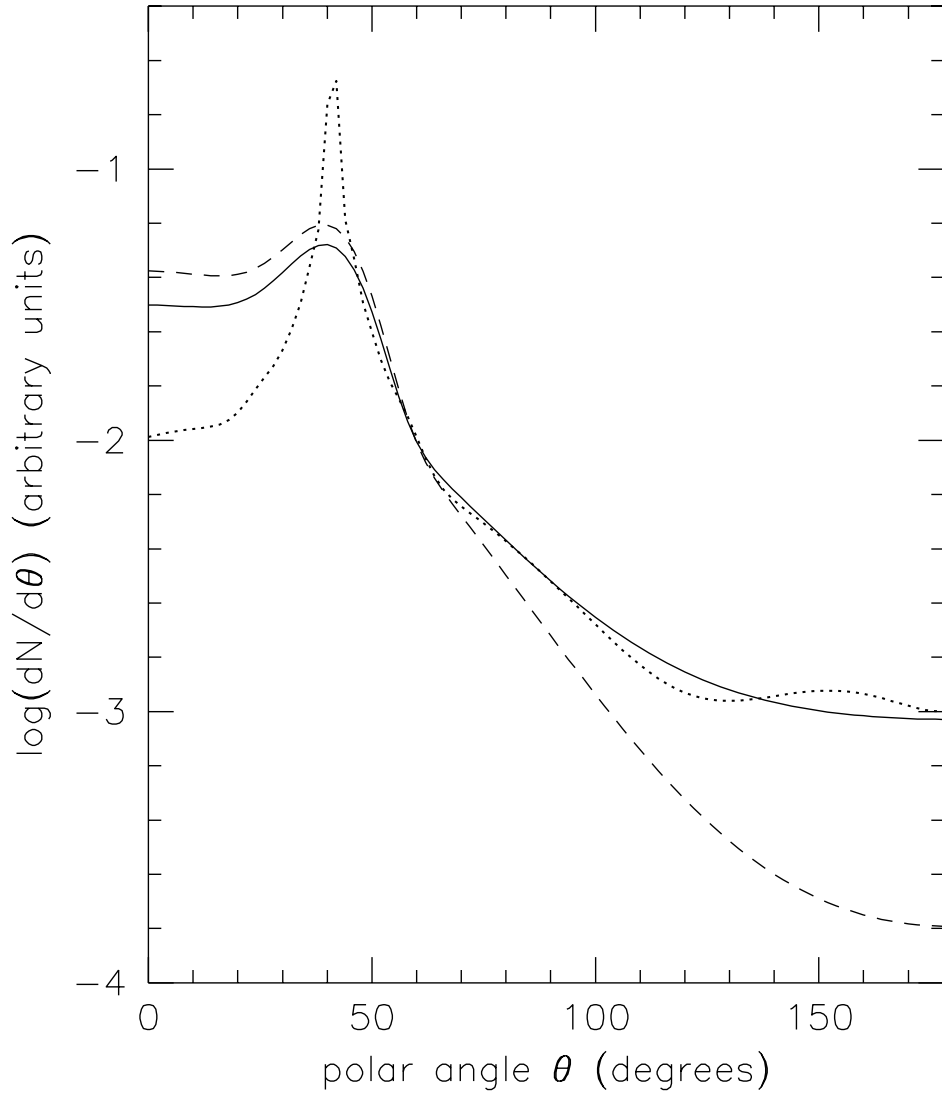


Fig. 5.— Different forms for the expected Čerenkov angular emission from a high energy cascade. The dotted curve is from Belyaev (pure electromagnetic); the dashed curve an electromagnetic shower, and the solid curve a hadronic shower. See text for details. All showers are at 6.3 PeV, viewed at large distance.

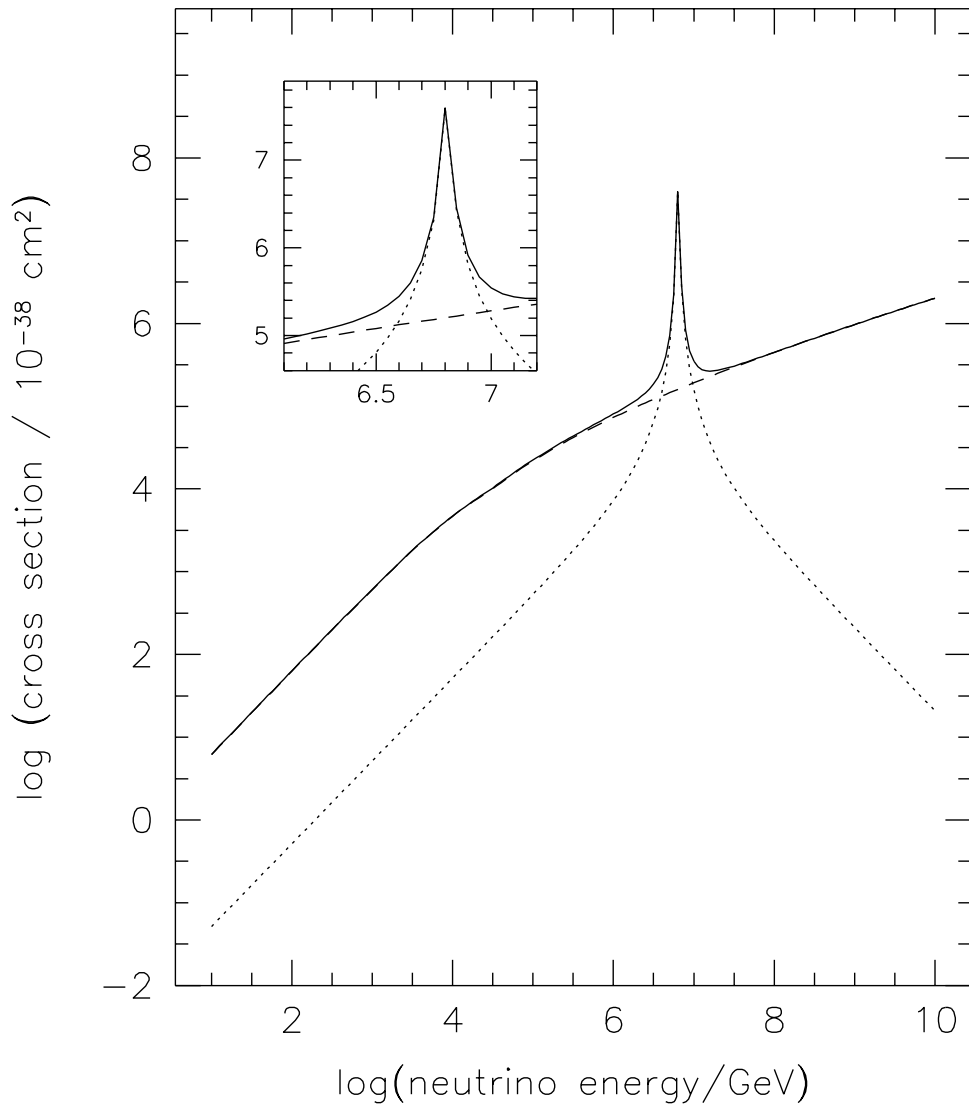


Fig. 6.— The Glashow resonance, with the electron antineutrino cross-section in dotted lines, the average deep-inelastic muon neutrino/antineutrino cross section in dashed lines and the total cross section in solid lines. The inset shows the detail near the resonance.

It should be noted that the standard model for the neutrino physics underlying these calculations is verified indirectly up to about 47 TeV by the HERA results on  $e^+p$  collisions (Gandhi, Quigg, Reno, and Sarcevic 1996).

#### 4.3.1. Scattering Monte Carlo and Results

In determining the statistical detector response to a large number of cascade or muon events, we have used an effective diffuse attenuation function which allows for a small additional scattering contribution, coming from very small angles relative to the direct beam from the shower. As discussed in a previous section, this approximately corrects for the difference between the beam and diffuse attenuation coefficients when using a detector with wide acceptance angles. However, such corrections do not treat the time delay effects that scattering introduces, especially at distances beyond  $L_{eff} \sim 300 m$ .

To ensure that the effects of the scattering and of the finite shower size and development time do not smear out the arrival times in such a way as to affect the sensitivity, we have simulated the effects of scattering upon the arrival of the light from great distances in the ocean using a three-dimensional Monte Carlo program which generates photon 4-vectors appropriate to a neutrino-induced cascade and includes Rayleigh scattering, particulate scattering, and absorption. The cascade angular distribution function is the same as that used in the main cascade Monte Carlo program, which is discussed above. A description of the methods used to develop the scattering Monte Carlo are given in Mobley (1994).

The program tracks individual photons by geometric optics and estimates scattering angles using the Petzoldt function discussed above, scaled to fit our data. Due to the intensive computational nature of photon tracking, it uses absorption and scattering values appropriate for the peak transmission wavelength,  $\sim 480 - 490 nm$ , where the overall number of photons has been normalized down to reflect this spectral window. This is a very good approximation at distances of many absorption lengths, since the light becomes nearly monochromatic at such distances.

Figure 7 shows results from this analysis for distances of 400 and 600 m from a shower, whose axis pointed at the detector center and was perpendicular to the string. The effective beam attenuation length (an input parameter) in this case was 44 m at 480 nm, where this is the geometric mean of scattering and absorption consistent with the measurements at our site. The events were used to investigate the time structure of cascade signals at great distances in triggering studies with the Monte Carlo.

In fact these distributions may be used to estimate the likelihood of a trigger for any detector with a given area and quantum collection efficiency. For our case, the combined effects of these and other factors give a sensitivity of order  $2 \times 10^{-2} pe$  per incident photon per  $m^2$ . Given the response time of our OMs, and the discriminator used, a 10 PeV cascade at a distance of 400 m would produce a trigger at about the 1.5  $pe$  discriminator level, but a 10 PeV cascade at a

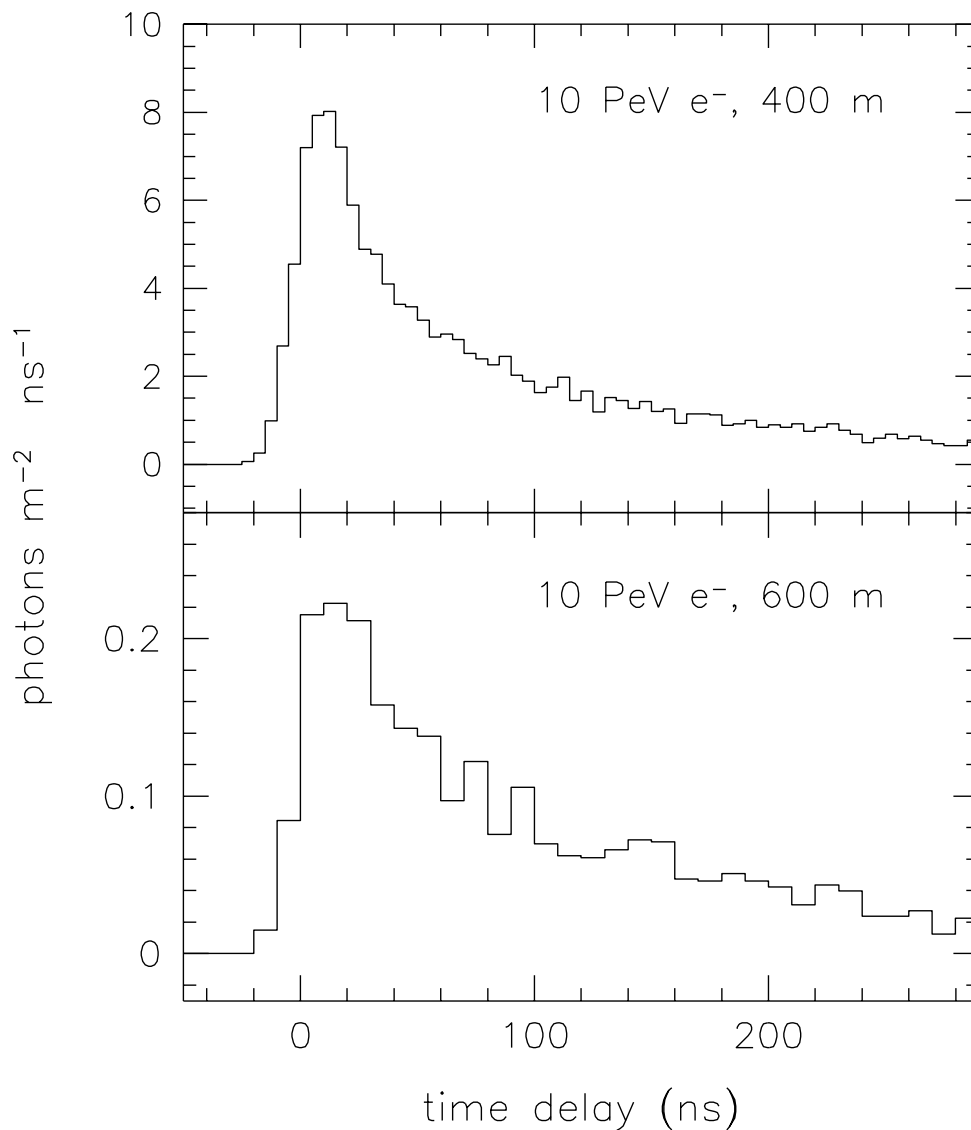


Fig. 7.— Simulated time delay effects of scattering of light from distant cascades. The top panel shows the arrival time distribution from an electron-initiated cascade at a distance of 400 m, for all photons arriving within 40 m of the detector center, in a plane which contains the detector string. The bottom panel is similar, for a distance of 600 m. Both events correspond to a total cascade energy of  $\sim 10$  PeV, with the shower axis pointing at the detector.

distance of 600 m would not trigger, as expected, since the threshold energy at this distance is much higher. This will be treated in a later section.

The plot shows the arrival time distribution for the detector plane within 40 m of the detector center. (The time difference due to wavefront curvature amounts to  $\leq 9$  ns across this disk at these distances). The risetime for both distributions is  $\sim 20$  ns, which is comparable to the risetime of the large area PMTs that were employed for the experiment. The duration of the pulse is  $\sim 40$  ns FWHM for the 400 m case, and  $\sim 80$  ns FWHM at 600 m. In either case the conditions for a trigger and accurate charge estimation are met: the risetime is comparable to the  $\sim 13$  ns risetime of the PMT (Hayashino 1990), and a major portion of the pulse arrives within the  $\sim$  few hundred ns OM LED pulse.

#### 4.4. Effective Mass Determination

##### 4.4.1. Cascades

The effective mass for cascades is determined by simulating a large number of uniformly distributed events over a region of sufficient volume so that the sensitivity is negligible outside it. The effective mass is then estimated by taking the ratio of detected to generated events as a function of the radial distance from the detector, and integrating it out to the edge of the generation volume.

Figure 8 shows the radial distribution of detected cascade events for 4 different simulation energies:  $10^1, 10^3, 10^5$ , and  $10^7$  TeV, in order of increasing maximum radius. The plot shows only the events for which 6 or more OMs were above the 5 pe threshold. At the highest energies, events are detected at distances of order twice the Rayleigh scattering length, as discussed above. The units of Figure 8 have been converted to effective volume by multiplying the volume of each radial shell by the triggering efficiency for the given shell and neutrino energy.

##### 4.4.2. Muons

The more conventional technique to search for cosmic neutrinos in deep detectors is to look for the high energy muons produced in charged current interactions around or below the horizon. The long range of these muons (a 100 TeV muon has  $\sim 13$  kmwe range) significantly increases the volume of target material scanned and thus, the sensitivity of the detector. Muons produced from neutrinos whose energies are greater than  $\sim 100$  TeV can be placed in roughly three categories:

- (i) Charged current muons via  $\nu_\mu + Nucleon \rightarrow \mu + Hadronic\ cascade$ . This is the bread and butter reaction for high energy neutrino detection. Note also that the resonant reaction  $\bar{\nu}_e + e^- \rightarrow W^-$  will also produce a muon  $\sim 11\%$  of the time from the decay of the W boson.

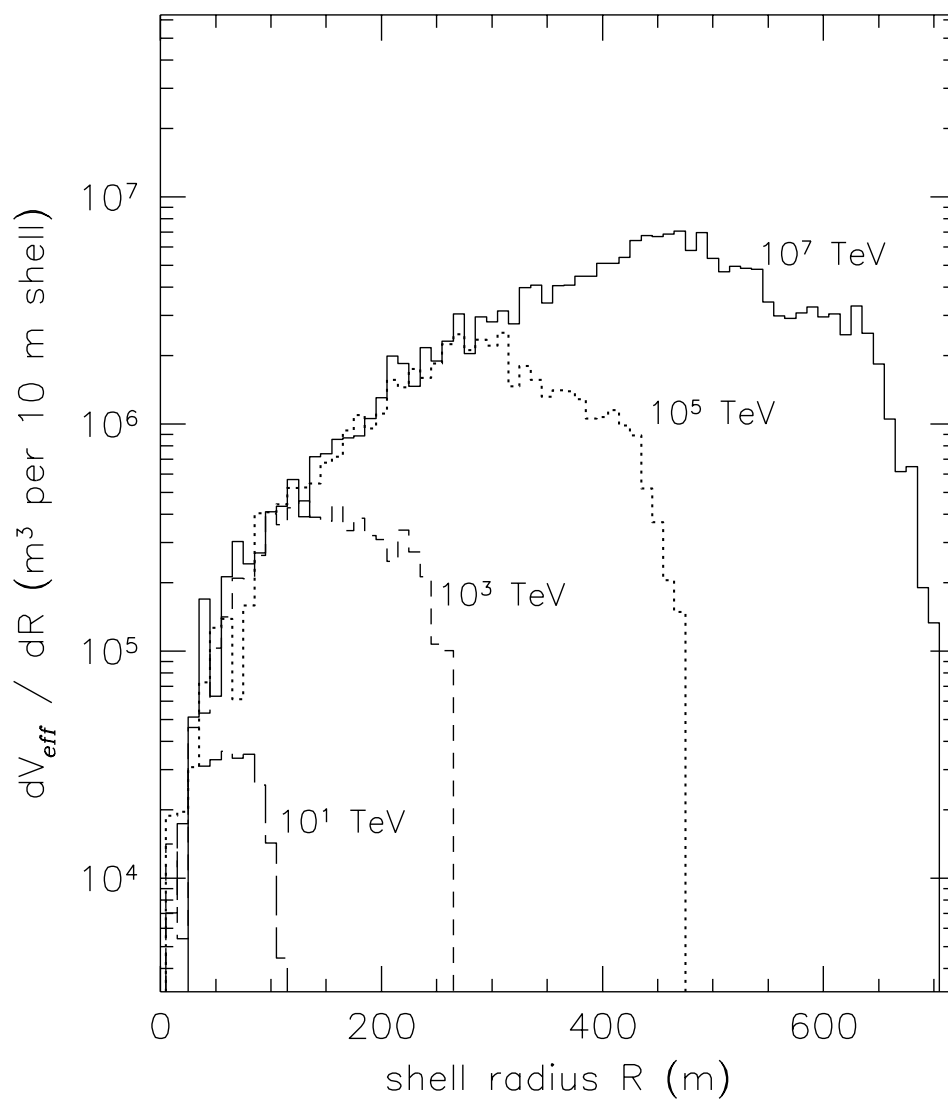


Fig. 8.— The differential effective volume of the detector as determined by Monte Carlo simulations as a function of radius, for the  $\geq 5$   $pe$  cut, as discussed in the text. Histograms correspond to neutrino energies of  $10^1, 10^3, 10^5, \& 10^7$   $TeV$  in order of increasing maximum event radius.

- (ii) Muons produced from the decay of heavier particles created in the hadronic cascade. Copious amounts of  $\pi$ 's and K's are produced in hadronic cascades however, the competition between decay and interaction in a dense medium like the ocean severely limits their decay both in number and energy. Moving to higher energies, charmed particles such as  $D^{\pm,0}$ ,  $D_s^{\pm}$  and  $\Lambda_c^+$  can produce muons (prompt muons) due to their very short ( $\sim 10^{-12}s$ ) life times, although the cross section for charm production and their branching ratios are small (and poorly known).

A crude estimate for the number of muons, if any, produced in hadronic cascades in sea water from the decay of  $\pi$ 's and K's was attempted by Jones (1976). He estimates that the number of decay muons is  $\sim 10^{-4} N_\pi$  where  $N_\pi = 0.8 E_c^{0.75}$ , is the number of stopping  $\pi$ 's, and  $E_c$  is the energy of the cascade in GeV. The following table is based on this expression.

$E_c$ (GeV)	$10^3$	$10^4$	$10^5$	$10^6$	$10^7$	$10^8$	$10^9$	$10^{10}$
$N_\mu$	0.014	0.08	0.45	2.5	14.2	80	450	2530

A few comments are in order about this estimate:

- The expression  $N_\pi = 0.8 E_c^{0.75}$  is 'well represented' for  $3 \leq E_c \leq 3000$  GeV. It is not clear how high in energy one can reasonably extrapolate this result however, it does scale like similar calculations made for the average number of muons in EAS (cf. Elbert 1978, Gaisser 1990).
  - The overall normalization is bounded on the high side by accelerator studies of 'punch through' muons and may, in reality, be much lower.
  - The number of muons in the above table is for  $\sim 20$  GeV minimum ionizing muons which range out in  $\sim 100$  m. As we show below, for the cuts used in this analysis, the SPS's effective area is essentially zero for all but the most vertical downgoing, high energy muons.
- (iii) Direct production of  $\mu$ 's in the cascade, e.g.,  $\gamma \rightarrow \mu^+\mu^-$ . Jones (1976), also notes that direct production processes also seem to be  $\sim 10^{-4} N_\pi$  and that the muons in hadronic cascades should be about twice the numbers quoted in the table above. Note that  $\gamma \rightarrow \mu^+\mu^-$  is suppressed relative to  $\gamma \rightarrow e^+e^-$  by about  $(m_e/m_\mu)^2 \approx 2 \times 10^{-5}$ .

Although the SPS was optimized for muon detection, the angular sensitivity of the detector was such that vertical muons (primarily from cosmic rays) were most likely to trigger, and the sensitivity to horizontal or upcoming muons was significantly less.

The top graph in Figure 9 shows a comparison of the effective area for isotropic muons with an  $E^{-2}$  energy spectrum as determined in the original analysis, Babson et al. (1990), compared with this analysis for the same  $E^{-2}$  input spectrum. The results are in good agreement with one another. We then examined the effective area as a function of the data cuts  $\geq 1.6$   $pe$  and  $\geq 5$   $pe$

as shown in the bottom graph of Figure 9. An estimate of the effective mass for muon detection is obtained by taking the effective area and multiplying by the muon range as a function of energy. As one can see, for the  $\geq 5 pe$  cut used to optimize cascade detection, the effective area for muons coming from zenith angles greater than  $\sim 40^\circ$  is negligible. Thus the effective mass for detection of neutrinos via the decay muons in cascades has been neglected since these must be observed near or below the horizon.

#### 4.4.3. Muons and Cascades from Charged Current Interactions

It is possible to detect very high energy muons indirectly through associated cascades via catastrophic energy loss along the muon track, which could produce a detectable cascade. However, since the energy of such a cascade is unlikely to be more than a small fraction of the primary neutrino energy, the additional sensitivity that this affords for detection of the primary neutrino flux is again much less than that of the initial hadronic or electromagnetic cascades.

Figure 10 compares the differential effective volume of detected cascade events with and without an exiting charged current muon at a *neutrino* energy of 1 PeV. The distributions for the  $\geq 5 pe$  cut are equal up to a radius of 230 m where the cascade dominates the signal. A transition region occurs around 230 m where the probability for neutrino detection transfers to the muon. The integral of the two distributions differ by 16% for the  $\geq 5 pe$  cut. Notice that the two distributions for charged current interactions (triggered and  $\geq 5 pe$ ) become equal at a radius of around 330 m, well beyond the distance where the light from the cascade can be detected. Further examination of these events revealed that they were from muons whose trajectories took them right above the detector where they registered a catastrophic energy loss. Muons originating from beyond 350 m failed to trigger the detector as the solid angle for such events becomes relatively negligible.

The techniques employed in our search for very high energy neutrinos are centered squarely upon the cascade. Focus is placed on the high detection probability for cascades compared to the relatively low detection probability for muons. The detection probability is simply a function of visible energy deposition per unit volume. As we showed above, the effective mass for muon detection, relative to cascade detection, is low indeed. However, muons in neutrino interactions may affect the sensitivity by producing bad fits to our cascade hypothesis and hence, reducing the effective mass. The worst case scenario for the fitting algorithms are the very high energy charged current muons ( $E_\mu \approx 0.7 \sim 0.8 E_\nu$ ) since these are producing cascades all along their trajectory throughout the sensitive volume. This subject will be addressed in a later section although it does not change the results.

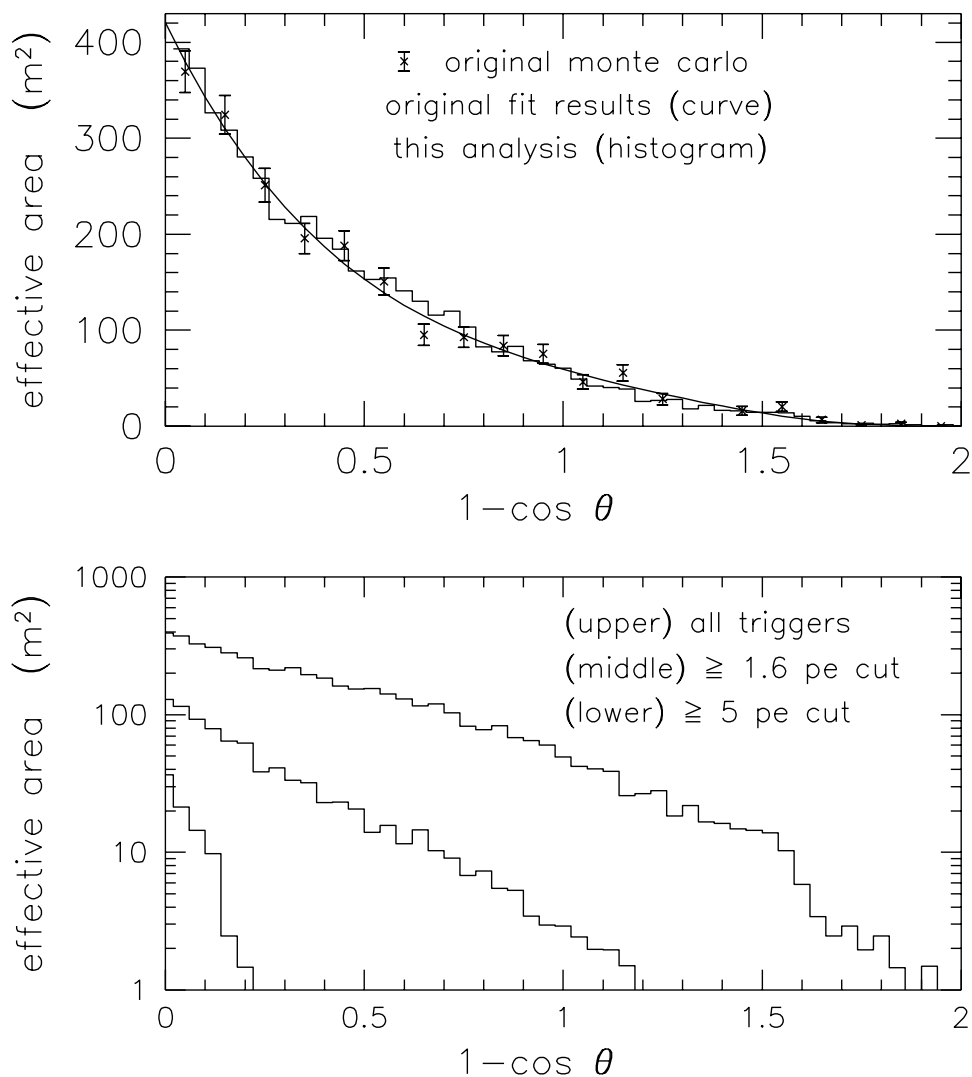


Fig. 9.— The effective area of the SPS for muons with an  $E^{-2}$  energy spectrum. The effective area is plotted against  $1 - \cos \theta$  so that the zenith is to the left of the graphs. The top graph provides a consistency check of our simulations with that of the original analysis, Babson et al.,(1990). The bottom graph shows the effective area for the data cuts used here. Note the effective area for the  $\geq 5$  pe cut is negligible for zenith angles greater than  $\sim 40^\circ$ .

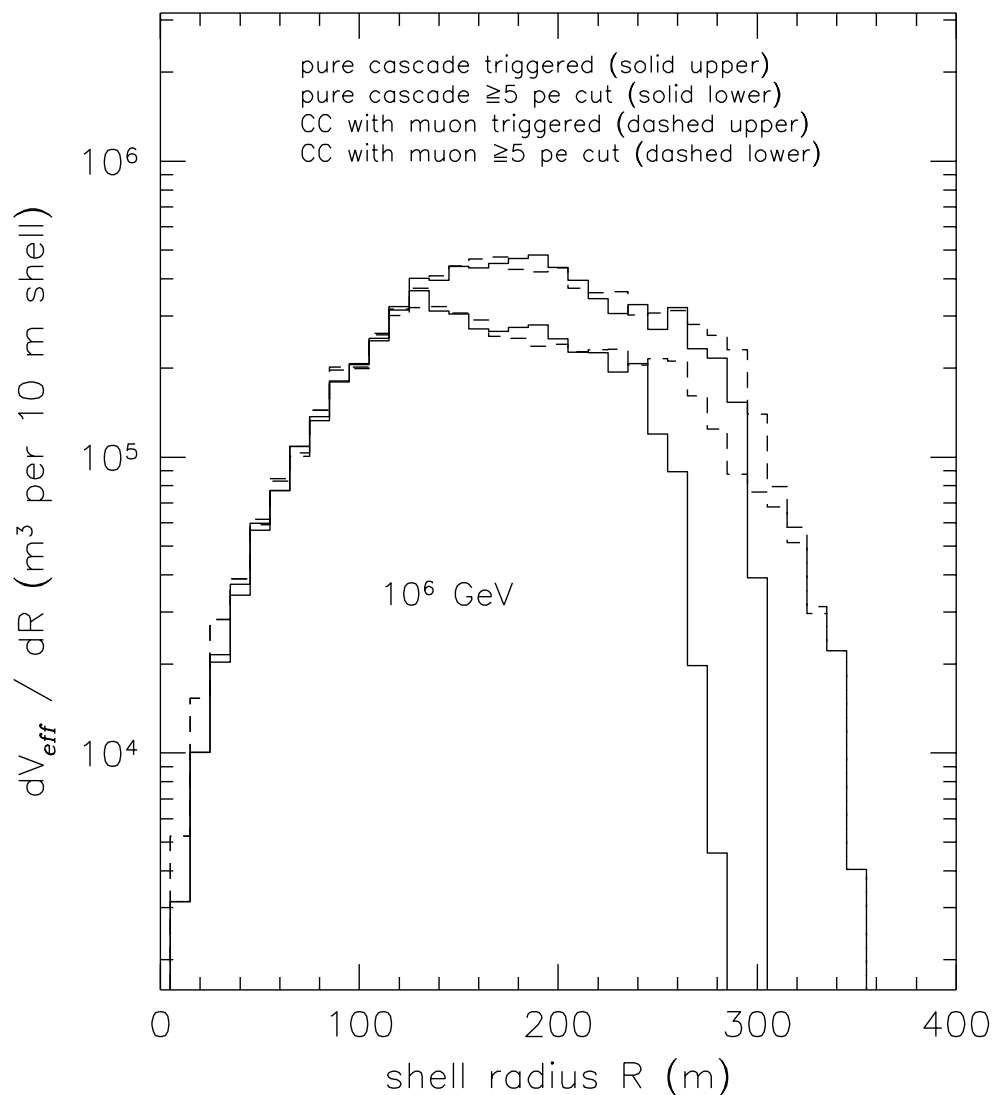


Fig. 10.— The differential effective volumes of detected cascade events with and without an exiting charged current muon at a *neutrino* energy of 1 PeV. The top two histograms are for events that triggered the detector. The bottom two histograms are for all events passing the  $\geq 5$  *pe* cut. The integral of the two  $\geq 5$  *pe* distributions differ by 16%.

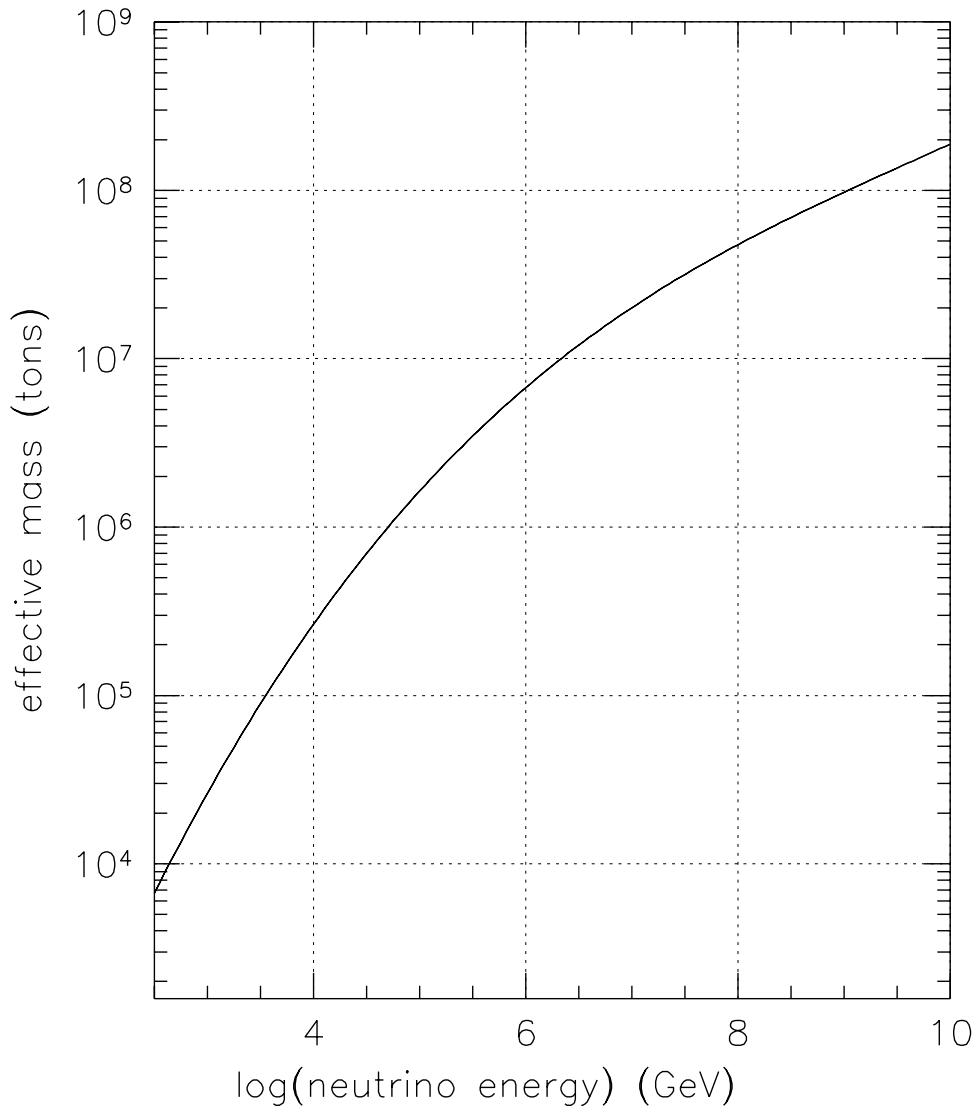


Fig. 11.— Effective mass of the SPS for neutrino detection as a function of neutrino energy, as determined by Monte Carlo calculations for conditions discussed in the text.

#### 4.4.4. Effective Mass for Neutrino Detection

The effective detector mass for neutrino detection estimated by our simulations is shown in Figure 11. The effective mass exceeds 10 Mtons at the energy of the Glashow resonance, and is of order 2 Mtons at 100 TeV, where the muon effective mass is of order 10% of this. At the highest energies, it approaches 200 Mtons, or 20% of a cubic kilometer of water.

We note that in general it is possible to achieve more sensitivity to neutrinos through muon detection, if the detector is optimized for such sensitivity. In our case, the relatively small number of OMs makes it difficult to adequately reconstruct the muon directions except for those which pass very near the detector. In contrast, the brightness of the cascades is what distinguishes them, and because the AGN neutrinos come from a diffuse source, we do not require high angular resolution in detecting them. For a detector with a greater number of OMs the muon sensitivity will improve rapidly and should eventually equal or surpass the cascade sensitivity (Reines 1978) as the number of OMs which detect the muon gets large compared to the number of fit parameters for muon tracks.

## 5. Results

### 5.1. Data Selection

Before beginning the analysis, we first simulated the distribution of expected cascade events based on the hypothesis of neutrinos from AGN according to the models of Bierman (1992), Szabo and Protheroe (1994), Stecker and Salomon (1996), Protheroe (1997). Based on these estimates we determined an *a priori* selection criterion for AGN neutrino-induced cascades: the event must produce  $\geq 5$  *pe* per module within the expected time coincidence window of the detector (160 ns). This criterion was modified to require at least a 6-fold coincidence (out of 7 OMs total) since in several data-taking runs only 6 OMs were active.

This requirement is much more restrictive than the SPS trigger which required  $\geq 0.8$  *pe* per OM and a 5-fold or greater coincidence. We also expected very few muon events to pass such a cut, since the average detected muon produces only 1-2 *pe* per OM and hits only 5 OMs. After careful simulation of all of the effects mentioned above, this cut was found to reject  $\geq 90\%$  of the atmospheric muons, while still accepting  $\sim 70\%$  of all of the cascades above 10 TeV. Thus we maintained this selection criterion throughout the analysis.

The number distribution of the effective minimum charge per event (accounting for the 6/7 cut in the small sample of 7-fold events recorded) for the 6-fold and greater events is shown in Figure 12. The dashed line shows our Monte Carlo prediction for atmospheric muons.

Analysis of the distribution around the threshold of 0.8 *pe* per OM for the formation of the initial hardware trigger is shown in the inset to Figure 12. Analysis of the steepening of the

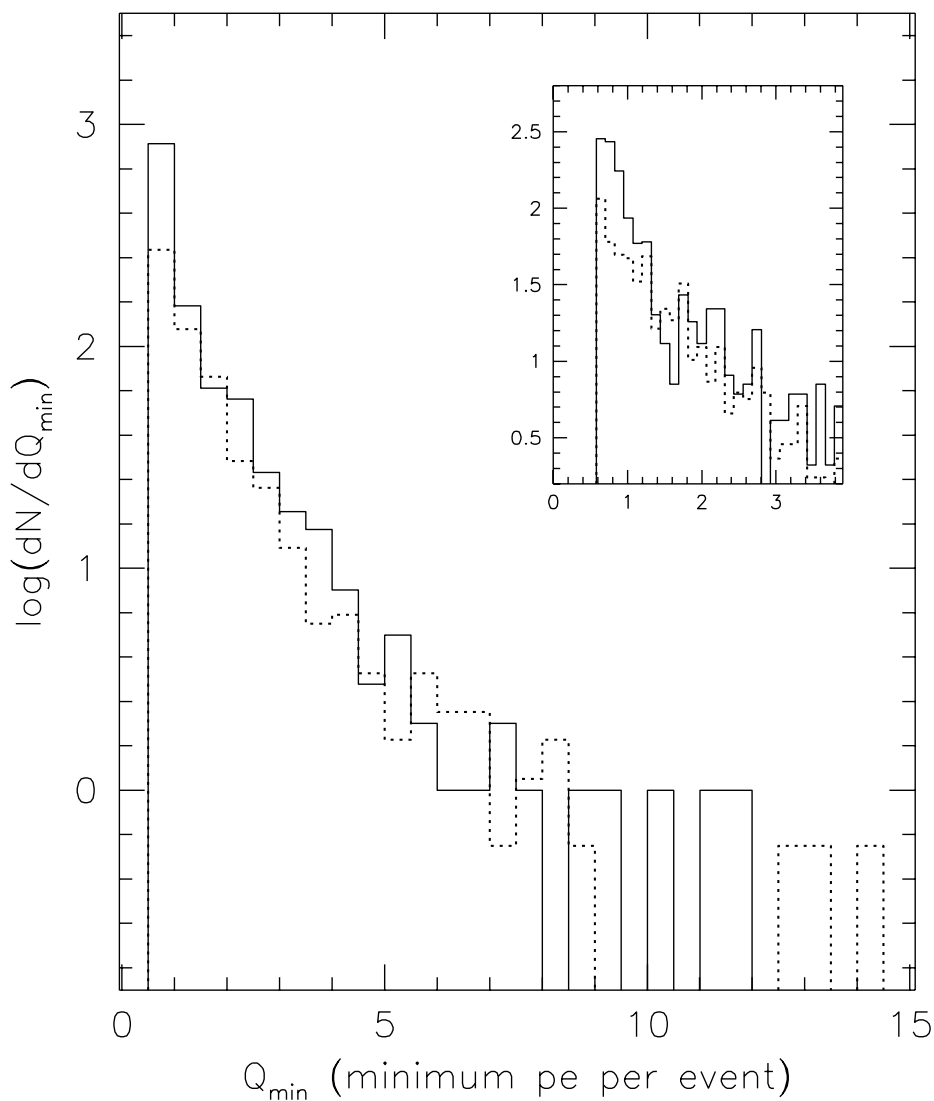


Fig. 12.— The number distribution of coincidence events with at least 6 OMs greater than the threshold  $Q_{min}$ , with the dotted curve showing the expected distribution from Monte Carlo calculations, with a simple model for phototube noise. The inset shows the distribution near the threshold where photomultiplier noise events become important in the sample, and the Monte Carlo approximation is less accurate. In the post-processing a threshold of 1.6  $pe$  per OM per event was used to isolate a relatively pure sample of muon events.

distribution below 1.6  $pe$  shows that these events are due to noise contamination. Since we wished to establish a pure sample of well-constrained muon events to act as a standard against which we can compare possible cascade candidates, we cut events which had less than 6 OMs above the 1.6  $pe$  threshold. The remaining events constituted our parent sample of what is expected to be mostly muon events with a possible sub-population of cascade events.

## 5.2. Characterization of Muon event sample

To identify the cascades we first characterized the parent distribution of muons, including all of those above the 1.6  $pe$  threshold, although most of them do not pass the more stringent 5  $pe$  cut required of cascades. This analysis serves to identify the angular distribution of the muons, the distribution of track impact parameters, and other aspects which may help to distinguish a cascade from the dominant muon population.

### 5.2.1. Muon fitting

The muon track parameters were estimated from the data using a likelihood function minimization (minimizing the exponent to maximize the likelihood). The log(likelihood function) is:

$$\ln(L) = \sum_{i=1}^7 \left( \frac{(t_i - T_i)^2}{\sigma_{t_i}^2} + EQ_i - q_i \ln(EQ_i) + \ln(\Gamma(q_i + 1)) \right) \quad (4)$$

where  $(t_i, q_i)$  are the measured arrival time and PMT charge,  $(T_i, Q_i)$  are the corresponding expected values,  $\sigma_{t_i}^2$  the estimated variance of the arrival time distribution, and  $E$  is a parameter, here designated the *energy parameter*, which estimates the brightness factor for a muon (or possibly multiple muon group) and is unity for a single, minimum-ionizing muon. The function assumes gaussian variance for the pulse arrival times, and Poisson variance for the PMT charge.

The cumulative probability curve for this likelihood function was estimated by a Monte Carlo integration, and fits which fell outside of  $\sim 2\sigma$  ( $\sim 4\%$  probability) were excluded to avoid contamination from events that contained pre-pulse, bremsstrahlung, or bioluminescence activity. Such events may still be fit if the outlier charge and time values are identified and removed from the fit, but in most cases this effectively reduces the coincidence level to a 5-fold, and the event is rejected. The fitting efficiency after this cut was  $\sim 70\%$ .

Figure 13 shows the fitted angular distribution of the muon tracks, plotted vs.  $(1 - \cos\theta)$  so that the zenith is at the left of the plot. The fitted Monte Carlo distribution is also shown for an average over our depths, plotted in dashed lines from the simulations, based on the parameterization of Okada (1994). Also plotted is the angular distribution of the events above

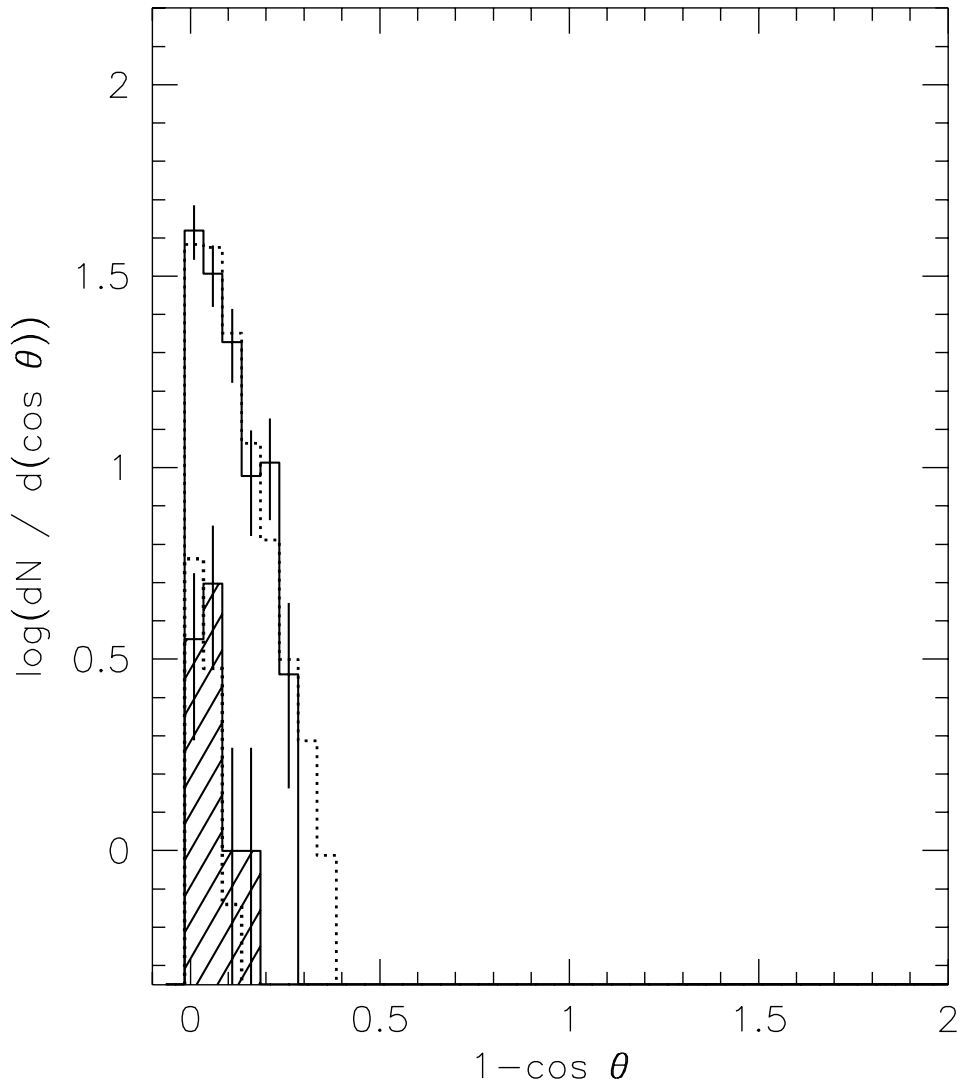


Fig. 13.— Fitted angular distribution of muon events. Solid line: parent sample with  $Q_{min} \geq 1.6$  pe. Hatched portion: the subsample with  $Q_{min} \geq 5$  pe. Dotted lines: fitted distribution from simulations of atmospheric muons.

the 5  $pe$  cut fitted as muon events, and the expected distribution in angle of these events from the Monte Carlo. Both samples are well-described by the hypothesis that they are muons coming from angles close to the zenith.

The track impact parameter is defined here as the distance of closest approach of the track to the center of the string. The fitted distribution is shown in Figure 14. The apparent mean value of the distribution for the  $\geq 5$   $pe$  sample is smaller than that of the total distribution. This is to be expected since most of the events in the subsample are in fact muons selected to be brighter because they have passed closer to the string axis than the average track. In Figure 14, the dotted lines show the Monte Carlo results for the same conditions. In both the  $\geq 5$  and  $\geq 1.6$   $pe$  samples, the data are consistent with the expected distributions from atmospheric muons.

We note that the results of fitting the energy factor  $E$  are consistent with a (multiple muon + catastrophic energy loss) event fraction of  $\sim 15\%$  in the parent muon data sample, and  $\sim 20\%$  in the high- $pe$  sample. The energy parameter provides an estimate of how well the photomultiplier charge distribution fits a single, minimum-ionizing muon, for which it is unity. The results of the fits to our data are consistent with our expectations from the Monte Carlo.

For our observation, the Monte Carlo estimate predicts that 8.8% of atmospheric muons which pass the 1.6  $pe$  cut should also pass the 5  $pe$  cut, corresponding to 18.7 events. We observed 17, consistent with no AGN neutrino cascade events present. After correction for obvious pre-pulse or other noise contamination in single OMs in 4 out of these 17 events, all of the 17 were fit to parameters consistent with atmospheric muons.

### 5.3. Testing for possible cascades

To provide an independent test for the presence of neutrinos in the high- $pe$  sample, we used a cascade likelihood fitting routine similar to that used to fit the muon track parameters applied to the entire probable muon event parent sample, to the subsample of those events above the 5  $pe$  threshold, and to the Monte Carlo generated neutrino events also above the 5  $pe$  threshold. This approach allows us to determine which, if any, distinguishing characteristics of AGN neutrino events may be differentiated by such a modest detector like the SPS.

#### 5.3.1. Fitting Monte Carlo Neutrino Interactions

The fits were computed assuming that the data represented measurements of the arrival of a Čerenkov wavefront from a cascade that appeared nearly pointlike to the detector. This approximation is reasonable since even cascades at very high energies have spatial dimensions of order 10 m or so along their length.

Since the SPS was a single string of OMs, along with the fact that it spanned a distance of

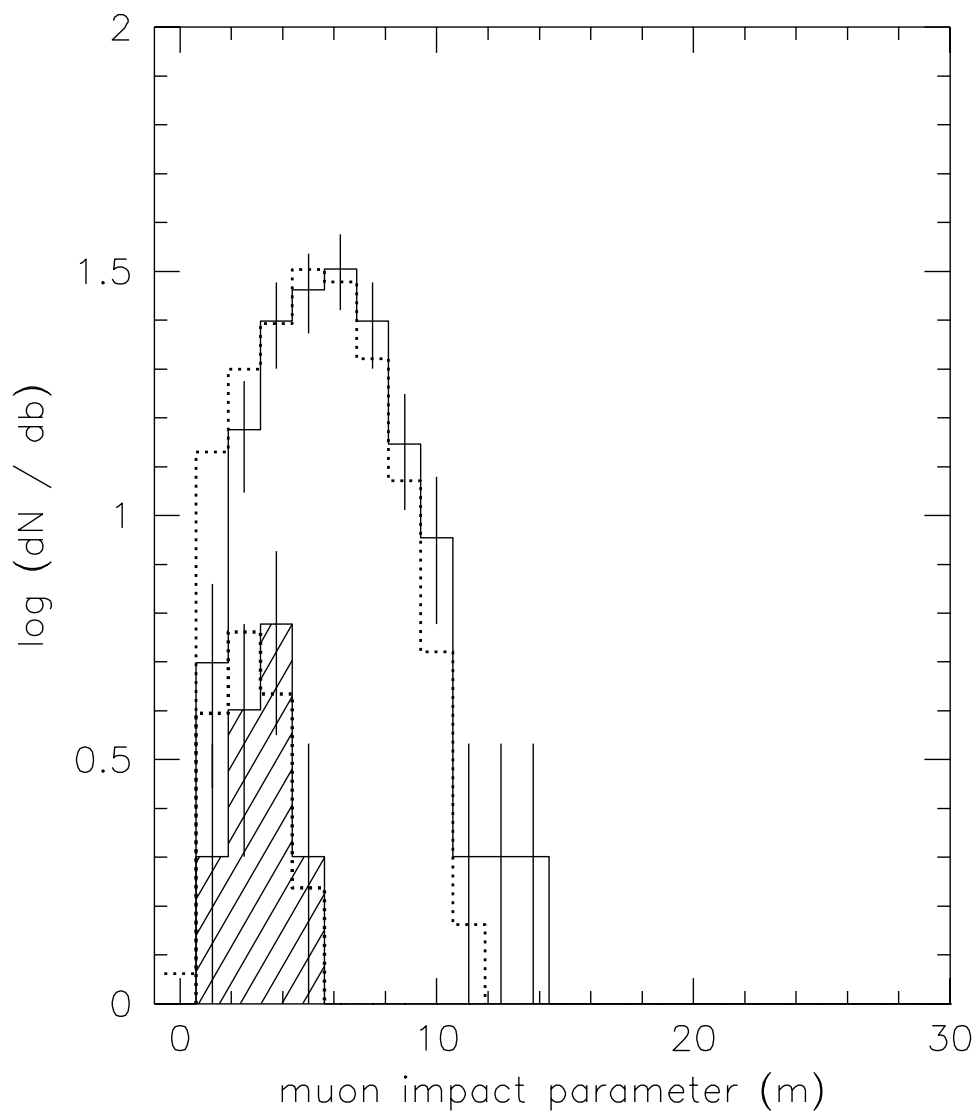


Fig. 14.— Fitted muon track impact parameter distribution. The impact parameter here is the distance of closest approach to detector center. Solid line: parent sample with  $Q_{min} \geq 1.6 pe$ . Hatched portion: the subsample with  $Q_{min} \geq 5 pe$ . Dotted lines: fitted distribution from simulations of atmospheric muons.

only  $\sim 30$  m, it simply did not have the moment arm required to reliably measure the range to a distant cascade vertex given the very large sensitive volume (see Figure 8). In fitting terminology, the topology in chi-square space for the range fit was just too flat and, consequently, a lagrange multiplier had to be added to keep the fitter from running away to unphysically large distances. This resulted in fits for the range to the cascade vertex to be clustered tightly around the initial guess. Furthermore, the energy estimation was equally erroneous, aside from the poor sampling, because it relies upon the distance to the cascade. What remained to distinguish the diffuse astrophysical neutrinos from the copious background of cosmic ray muons was their brightness and angular distribution.

As we show below, the isotropic angular distribution (outside of Earth) proved to be a *robust* signature of the diffuse neutrinos from AGN. Another source of isotropic neutrinos (for energies  $\leq 10^7 \sim 10^8$  GeV) are the atmospheric charm produced neutrinos. For a discussion of this potential background, the reader is directed to Hill (1996), and references therein. We suffice it to say here, that only for the highest model of charm production that is consistent with both accelerator data, and X-ray chamber measurements of the vertical muon flux up to 50 TeV, the lowest AGN flux prediction of Protheroe (1997), may be difficult to measure without ambiguity.

### 5.3.2. OM Saturation

As discussed in an earlier section, the SPS OMs would begin to saturate at about 36 *pe*, and would be in full saturation at  $\sim 300$  *pe* (see Figure 4). In order to assess how OM saturation may affect our result, several different scenarios and fitting algorithms were developed:

- Fitting with both realistic time and ideal charge. The charge measurement was simulated from ideal OMs that could measure an infinite amount of charge without saturating. The timing information was simulated as in the real detector.
- Fitting with both realistic time and realistic charge. The charge measurement was simulated to be from the SPS OMs (see Figure 4). The error of charge measurement associated with saturated OMs ( $\geq 80$  *pe*) was taken to be necessarily large ( $10^4$  *pe*) in the likelihood function.
- Fitting with realistic time and realistic charge. Charge measurements in excess of  $\sim 80$  *pe* were removed from the fit.
- Fitting with realistic time only. The charge information enters only indirectly through the associated timing corrections for the constant risetime of the PMT TOT pulse (pulse height slewing).

Furthermore, several different minimization methods (conjugate gradient, powell’s method, grid search) were also tested. The above methods all produced the same angular distributions and all

had about the same fitting errors: median ( $\delta\theta_V$ )  $\approx 9^\circ \sim 10^\circ$ . The most notable differences was in the computing time.

### 5.3.3. Charged Current Muons with Cascades

Figure 15 shows the results of fitting neutrino events, with and without a charged current muon, to a cascade hypothesis. The top graph is the fitted angular distributions for the  $\geq 5$   $pe$  cut. There is a slight enhancement at the zenith for events with a charged current muon (suppressed by the logarithmic scaling). This enhancement is from muons whose trajectories were above the detector where they registered a catastrophic energy loss. The bottom graph is the associated fitting error in  $\cos \theta_V$  for the above distributions. The fitting error is a little misleading for the events with a muon since  $\theta_V$  is *defined* as the angle to the neutrino interaction vertex, which is different from the angle to the muon induced cascade (call it  $\cos \theta_{\mu,casc}$ ) that was *detected*. The point to be made here, is that the fitted angular distributions for events with and without muons are, for identical likelihood cuts, virtually the same. The fitting efficiencies for the two distributions were 70.1% and 70.8% respectively.

### 5.3.4. Searching the Data for Cascades

The expected differences between a cascade and muon event for individual events could be small enough as to make them difficult to distinguish for a one-dimensional detector. In fact, there is at least one near-degeneracy in the fitting comparison: a minimum-ionizing muon coming from near the zenith, nearly parallel to the string axis, will produce a series of hits on the OMs which can appear similar to the near-plane-wave coming from a bright, distant cascade with a vertex zenith angle  $\theta_V$  (measured from the center of the detector to the cascade vertex) which is close to the muon Čerenkov angle. The major detectable difference between the two is in the gradient of the intensity: the muon intensity may have a flat distribution of detected  $pe$  (or large fluctuations if there is a bremsstrahlung or nuclear scattering event along the track), whereas the cascade light will fall off smoothly with distance as it is attenuated by the ocean and by the radial gradient.

The results of fitting both the parent muon sample and the high  $pe$  subsample to the cascade hypothesis are shown in Figure 16, where the angular distribution of  $(1 - \cos \theta_V)$  is plotted for both samples. The plot shows that the cascade fits favor a range of zenith angles clustered around the muon Čerenkov angle for vertical tracks. The high  $pe$  distribution shows no deviation from the parent distribution. Thus both samples appear to be dominated by nearly vertical muon events, consistent with expectations. For comparison, we have also fit a set of simulated atmospheric muon events (dotted histogram) and these show a distribution consistent with the data.

Also plotted in Figure 16 is the fitted distribution of vertex angles for simulated cascades from a typical AGN model with uniform angular intensity outside Earth, and a typical  $\nu_e$  to  $\nu_\mu$

fraction. We have used the matter attenuation models of Gandhi et al. (1996) to determine the effect of earth attenuation. It is clear that the fitted events do not appear to be drawn from the cascade distribution, either in the high  $pe$  sample or the larger parent sample.

No evidence for any AGN–neutrino–induced cascades is found in our data, either from the presence of an excess above background, or from the angular distribution of the events which comprise the most likely candidates for cascades. In all cases the data are completely consistent with atmospheric cosmic–ray muon events.

#### 5.4. Limits on AGN neutrinos

Based on the lack of evidence for any events that suggest the presence of a neutrino signal, either in the counting statistics or in the fitting of the individual events, we establish the limit by the 90% confidence level Poisson–statistics prescription of a maximum allowed signal flux of 2.3 counts above our estimated minimum detectable flux. This provides a limit that may be compared with the EAS-TOP limit (Agietta et al. 1994), in which 7 events were observed with 11 expected, also consistent with background.

The limit, plotted in Figure 17, is based on our Monte Carlo estimates of the effective volume  $V_{eff}(E_\nu)$  of the detector and the integrated solid angle  $\Omega_{eff}(E_\nu)$  over which it is sensitive, both of which are a function of the primary neutrino energy  $E_\nu$ . Because the typical AGN neutrino model predicts that the ratio of the number of electron neutrinos to muon neutrinos (and antineutrinos) is of order 1/2, we have estimated the differential under this assumption. Thus, for example, the flux of anti-electron neutrinos  $\bar{\nu}_e$  will be  $\sim 1/6$  of the total neutrino flux. Tau neutrinos are not expected to appear in significant numbers under present AGN models, as the neutrinos are from pion decay, and we do not include them here.

The differential limit is then estimated as:

$$\frac{dF_\nu}{d\log_{10}(E_\nu)} \leq \frac{N_{90\%CL}}{[P_n(E_\nu) + P_e(E_\nu)][V(E_c)\langle\Omega(E_\nu)\rangle] \tau} \quad (5)$$

where

$$P_n(E_\nu) = \rho N_{nucl} \langle\sigma_{\nu,H}(E_\nu)\rangle, \quad (6)$$

and

$$P_e(E_\nu) = \frac{10}{18} \rho N_{nucl} \langle\sigma_{\nu,e}(E_\nu)\rangle. \quad (7)$$

Here  $dF_\nu/d\log_{10}(E_\nu)$  is the differential neutrino flux in units of  $cm^{-2}s^{-1}sr^{-1}$ ;  $E_\nu$  is the

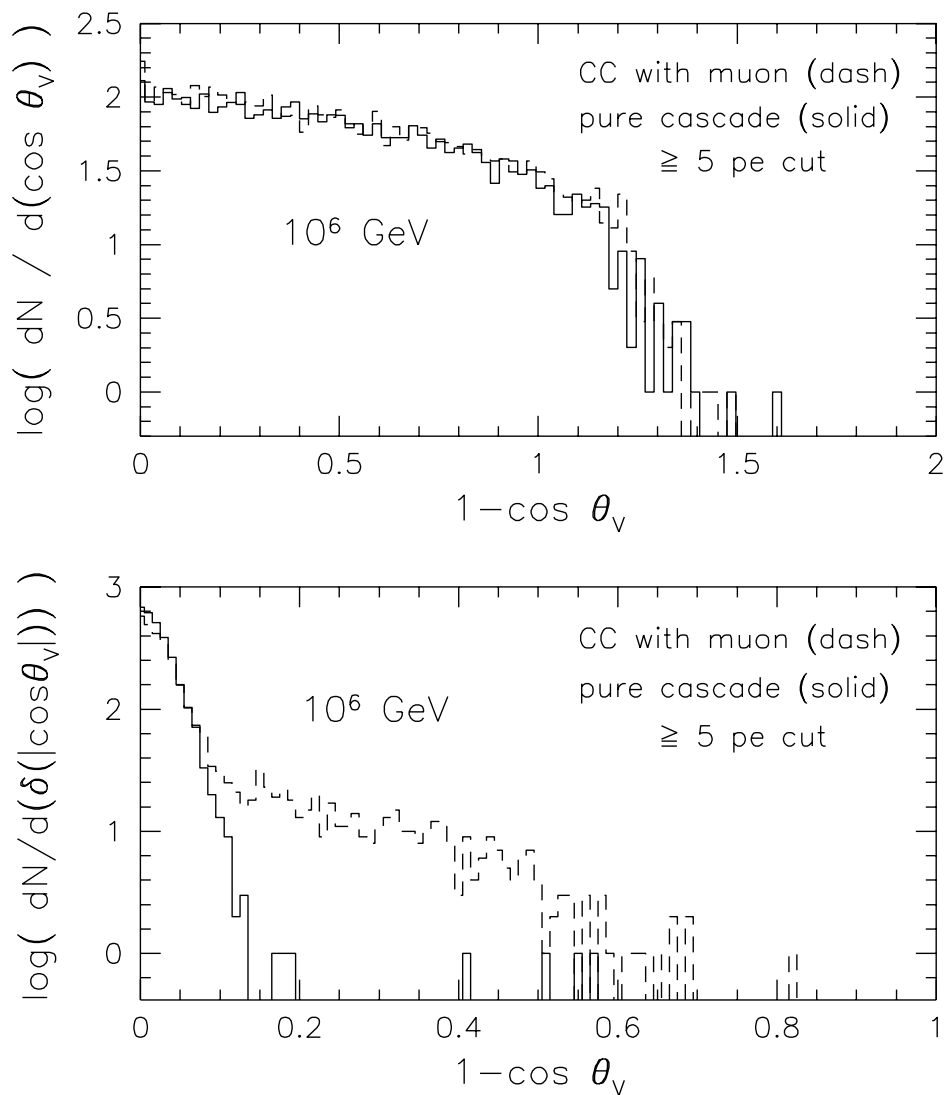


Fig. 15.— A comparison of neutrino events, with and without a charged current muon, fitted to a cascade hypothesis. The top graph is the fitted angular distributions for the  $\geq 5$  pe cut. The bottom graph is the associated fitting error in  $\cos \theta_V$  for the above distributions. The fitting error is a little misleading for the events with a muon since  $\theta_V$  is *defined* as the angle to the neutrino interaction vertex, which is different from the angle to the muon induced cascade (call it  $\cos \theta_{\mu,casc}$ ) that was *detected*. See text for details.

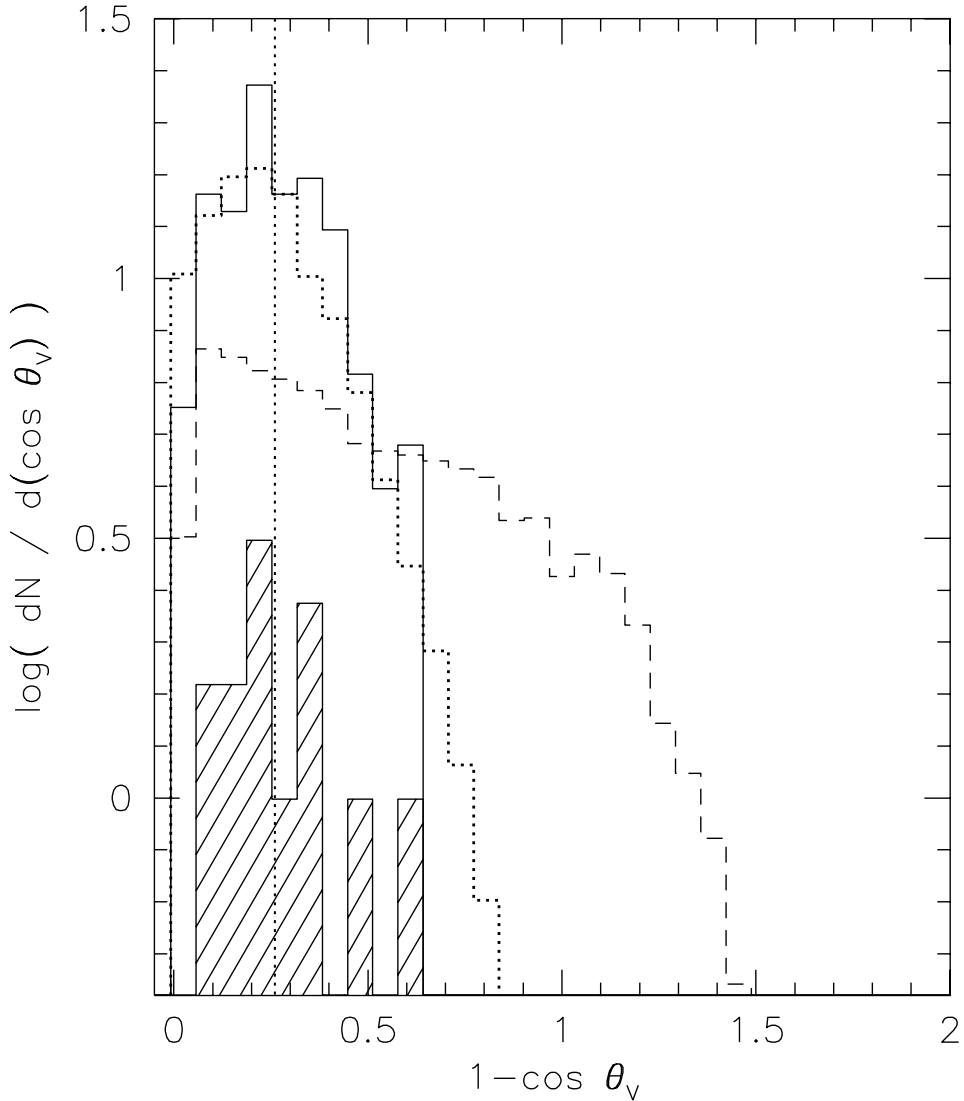


Fig. 16.— Angular distribution of events after fitting to a cascade hypothesis. The solid line is the distribution of the fits of the parent muon sample; the hatched portion that of the high- $pe$  subsample. The vertical dotted line indicates where the Čerenkov angle for vertical muons falls in this plot. The dotted histogram which lies near the fitted-muon distribution is the equivalent fitted distribution of simulated atmospheric muons. The short-dashed histogram indicates the expected distribution of cascade events from AGN neutrinos, normalized to the number of events in the  $\geq 1.6 pe$  sample. The plot shows that none of the data distributions appear to behave like the expected cascade distributions under a cascade hypothesis; in fact they behave exactly as expected from a distribution of atmospheric muon events.

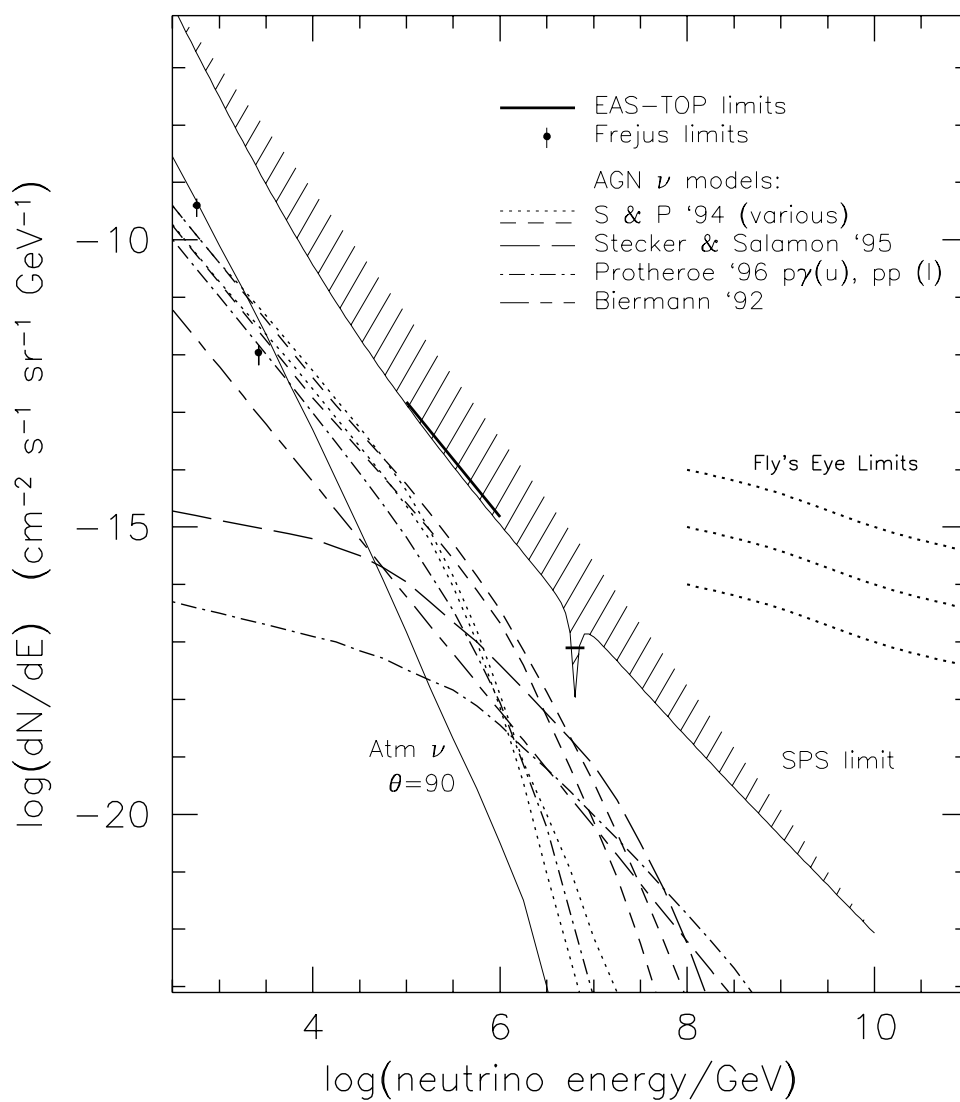


Fig. 17.— The limit derived here (“SPS limit”) is plotted along with a number of neutrino models and other limits. See text for details.

incident neutrino energy;  $N_{90\%CL} = 2.3$  is the maximum allowed flux at the 90% confidence level;  $V(E_c)$  is the effective volume of the detector for the high threshold cut, as a function of the cascade energy  $E_c$ ;  $\langle\Omega(E_\nu)\rangle$  is the average effective solid angle of the detector for the cut, as a function of neutrino energy, assuming the earth-attenuation parameterization of Gandhi et al. (1996); and  $\tau$  is the detector livetime (18.6 hours). We note that the effective solid angle is nearly  $4\pi$  at low energies for all neutrinos, then decreases to  $\sim 2\pi$  at energies above  $10^3$   $TeV$  as the neutrinos begin to suffer strong attenuation through the earth. (Note that the solid angle here involves the AGN neutrino source distribution, not the detector response which is already implicit in the calculation of the detection volume).

The cascade energy  $E_c(E_\nu)$  is estimated by taking an average over the Bjorken  $y$  distributions given by Gandhi et al. for the different flavors and interactions involved. In a similar way, the interaction probabilities  $P_n$ ,  $P_e$  for hadronic and electronic interactions use flavor- and/or particle-antiparticle-averaged cross sections  $\langle\sigma_{\nu,H}(E_\nu)\rangle$ ,  $\langle\sigma_{\nu,e}(E_\nu)\rangle$ . The average includes neutral- and charged-current interactions and assumes the flavor ratios discussed above. The factor  $\frac{10}{18}$  gives the approximate electron-to-nucleon ratio in seawater, and  $\rho N_{nucl} = 1.028 \times (6.03 \times 10^{23})$  nucleon  $cm^{-3}$  for deep ocean water.

In Figure 17 we also plot a number of suggested models, as well as atmospheric neutrino spectra, and limits from the underground muons observed by the Frèjus collaboration (Rhode et al. 1996) and the extensive air-shower limits given by the EAS-TOP experiment (Aglietta et al. 1994; 1995). The limits from the Fly’s Eye (Baltrusaitas et al. 1985) apply for three different assumed cross sections for  $\nu_e$  interactions in the atmosphere:  $\sigma_\nu = 10^{-31}$   $cm^2$  (uppermost limit),  $10^{-30}$   $cm^2$  (middle limit), and  $10^{-29}$   $cm^2$  (lowest limit). In each case the cross section is assumed constant for  $10^8 \leq E_\nu \leq 10^{11}$   $GeV$ . The cross sections used by Baltrusaitas et al. appear to be about an order of magnitude higher than those estimated by Gandhi et al (1996).

The AGN neutrino models shown are from Szabo and Protheroe (1994; S & P in the figure), Stecker and Salamon (1996), Protheroe (1997), Biermann (1992) and are a representative sample of those available. The Frèjus limits, based on measurements of horizontal muon events, appear to eliminate the highest flux models of Szabo and Protheroe (1994). Also shown here is the expected horizontal flux from atmospheric neutrinos, from Lipari (1993).

The limit at the W resonance has been appropriately scaled to account for a different effective solid angle because of the severe attenuation of these electron neutrinos passing through the earth, and for the typical ratio of electron to muon neutrinos in the models. The limit at this energy is:

$$\frac{dF_\nu}{dE_\nu}(6.3 \text{ PeV}; \text{AGN } \nu) \leq 1.1 \times 10^{-18} \text{ cm}^{-2} \text{ s}^{-1} \text{ sr}^{-1} \text{ GeV}^{-1}. \quad (8)$$

This is the most stringent limit at this energy and improves on the existing EAS-TOP limit by about a factor of 7.

Our value for the limit assumes that the electron neutrino+antineutrino to muon antineutrino+neutrino ratio is  $\sim 0.5$ , as most models predict, and that there is no significant

particle–antiparticle asymmetry. At the resonance energy, the model– *independent* limit for anti-electron neutrinos is more stringent:

$$\frac{dF_\nu}{dE_\nu}(6.3 \text{ PeV}; \text{mod. indep.}) \leq 3.2 \times 10^{-19} \text{ cm}^{-2} \text{ s}^{-1} \text{ sr}^{-1} \text{ GeV}^{-1}. \quad (9)$$

If we use a more conservative approach to establishing the limit, by assuming that the 17 observed events could include a possible signal (though no evidence was seen for this in event–by–event analysis) then the 90%CL limits are 2.6 times higher than quoted. However we note that this prescription is not consistent with the approach of Aglietta et al. (1994) and the limits cannot be accurately compared in this case.

## 6. Discussion

We find it quite remarkable that a modest detector can achieve such a large sensitive mass, though not designed nor optimized for this use. This instrument, intended merely as a proof-of-concept for a deep-ocean muon tracking instrument, has within less than 1 day’s total livetime produced the first limits at these high energies which begin to approach the predictions of the AGN neutrino models.

We note that in principle such a detector can also fit the incoming direction of the neutrino, by fitting the gradient of the distribution of the emitted Čerenkov light. However, with only seven sampling points separated by 5.2 meters, the constraints are inadequate to break the possible degeneracies in solutions to the fitted parameters. A larger detector could, however, achieve reasonable angular resolution as a cascade telescope, which would complement a more fine-grained muon-tracking detector.

### 6.1. W Resonance

It is evident from Figure 17 that the W resonance provides a spectral window of very high sensitivity, and if there are AGN electron antineutrinos present at numbers comparable to muon neutrinos, this will be the energy at which they are likely to be first detected. For this reason, future detectors should be optimized to achieve the highest possible sensitivity in this portion of the neutrino energy spectrum.

It may appear surprising that the our limit improves over the EAS-TOP limit to a greater degree at the resonance than at the lower energies; this is due mainly to the fact that the air shower detector must be within the shower itself, and the shower length grows only as the logarithm of shower energy. In our case, the Čerenkov emission grows linearly with the shower energy, and leads to an effective volume which grows more quickly with energy.

It will be of great value for further studies to be done on the distribution of Čerenkov light from a 6.4 PeV shower, since this will be crucial in determining the energy and direction of such events if they are seen. Additional research involving the Landau Migdal Pomeranchuk (LPM) effect, (Landau and Pomeranchuk 1953; Migdal 1956) is also needed. Although we have neglected the LPM effect in this paper, we note that this effect may *increase* the effective detection volume, especially for electromagnetic cascades, as the shower length becomes comparable to the optical attenuation length of the medium, (J. Alvarez-Muñiz and E. Zas 1997).

## 6.2. Extrapolation & Comparison

It appears that there may be other possible limits which can be estimated from air shower data or from further work with the Fly’s Eye (cf. Elbert and Sommers 1995), though interpretation of such limits is complicated by the possibility that the primary particles could be something other than a neutrino. Halzen and Zas (1992) showed that the measured fluxes of showers with large particle numbers from the AKENO air shower array is inconsistent with two early models for AGN neutrinos, but this was not directly converted to a neutrino flux limit, and the two early models were later shown to be inconsistent with X-ray data that were part of the input to the models.

We note that AMANDA (Antarctic Muon and Neutrino Detector Array) may be able to achieve comparable sensitivity in the near future (cf. Barwick et al. 1996). However, the much shorter effective scattering length in the deep ice (of order 30 m compared to  $\sim 300$  m in the deep ocean) complicates the reconstruction of cascade positions and other parameters and it remains to be seen what effective mass can be achieved with a deep ice detector operated in this mode.

The planned NESTOR detector, although optimized for lower energies, should be also quite effective as a cascade detector, and the clarity of Mediterranean water appears to match that of the observations here (cf. Resvanis et al. 1995). The DUMAND II instrument, for which the SPS experiment was intended to lay the groundwork, would have had an effective mass about an order of magnitude larger than the SPS, even in its first phase (3 strings of 24 OMs each). Either this or the NESTOR detector would begin to test some of these models within a few weeks’ operation. In contrast, the currently operating Baikal detector (Belolaptikov et al. 1995) suffers from a high level of scattering and absorption in the  $\sim 1$  km-depth lake water, as well as the problems of the high cosmic ray backgrounds from the shallow depth, and strong seasonal bioluminescence. These effects will limit its ability to detect cascade events, although it has proven to be an efficient muon telescope.

## 7. Conclusion

We have reanalyzed data from a deep ocean muon tracking experiment, the Short Prototype String, to search for evidence of high energy particle cascades which might be induced by neutrinos

from active galactic nuclei. The experiment was found to have a very large effective detection mass, greater than 1 Mton above 20 TeV and up to  $\sim 200$  Mton at  $10^7$  TeV, a fifth of a cubic kilometer. Because of the large effective mass, even a short observation of  $\sim 20$  hours livetime is adequate to set a new high-energy limit to the presence of a flux of neutrinos from AGN. Although the sensitivity in this observation was not yet adequate to detect the predicted fluxes, we have shown that the power of these techniques can and should be exploited as soon as possible to test these AGN models in a relatively short time.

We wish to thank Diane Ibaraki for her help recovering the data, and Sandip Pakvasa for useful discussions. This work was supported in part by the U.S. Department of Energy, the Japan Ministry of Education, and the Swiss National Science Foundation.

## REFERENCES

- Aglietta, M. et al., 1994, *Physics Letters B* **333**, 555.
- Aglietta, M. et al., 1995, *Proceedings of the 24th International Cosmic Ray Conference*, (Rome: IUPAP) vol 1, 638.
- Ahlen, S., Ambrosio, M., Antolini, R., et. al., 1992, *Physical Review D* **11**, 4836.
- Alvarez-Muñiz, J., and Zas, E., (1997), astro-ph9706064
- Babson, J. F. et al., 1990, *Physical Review D*, **42**, 3613.
- Baltrusaitas, R. M. et al., 1985, *Physical Review D* **31**, 2192.
- Belolaptikov, I. A. et al, 1995, *Proceedings of the 24th International Cosmic Ray Conference*, (Rome: IUPAP) vol 1, 789.
- Belyaev, A. A., Ivanenko, I. P., and Makarov, V. V., 1976, *Proceedings of DUMAND Summer Workshop*, ed. A. Roberts, (Honolulu, Univ. of Hawaii), 563.
- Berezinsky, V. S., 1977, *Proceedings of Neutrino 77*, M. A. Markov, G. V. Domogatsky, A. A. Komar, A. N. Tavkhelidze, eds., Baksan Valley, (Moscow: Institute for Nuclear Research) vol 1, 177.
- Biermann, P., 1992, *Proceedings of the Workshop on High Energy Neutrino Astrophysics (HENA)*, V. Stenger, J. Learned, S. Pakvasa and X. Tata, eds., Hawaii, 23-26 March 1992, (Singapore: World Scientific), 86.
- Clem, J., 1990, unpublished doctoral dissertation, Vanderbilt University, Nashville, Tennessee, U.S.A.
- Elbert, J. W., 1978, *Proceedings of the 1978 DUMAND Summer Workshop*, ed. A. Roberts, (Honolulu, Univ. of Hawaii) vol 2, 101.
- Elbert, J. W, and Sommers, P., 1995, *Astrophysical Journal*, **441**, 151.

- Gaisser, T. K., 1990, *Cosmic Rays and Particle Physics*, Cambridge, 207.
- Gaisser, T. K., Halzen, F., and Stanev, T., 1995, *Physics Reports* **258**, 173.
- Gandhi, R., Quigg, C., Reno, M. H., Sarcevic, I., 1996, *Astroparticle Physics* **5**, 81.
- Glashow, S. L., 1960, *Physical Review B*, **118**, 316.
- Halzen, F., and Zas, E., 1992, *Physics Letters B* **289**, 184.
- Hayashino, T., 1990, *Proceedings of The DUMAND Optical Module Workshop*, eds. S. Tanaka and A. Yamaguchi, (Sendai: Tohoku Univ.), 30.
- Hong, J. T., et al. (MACRO Collaboration), 1994, *Proceedings, Very high energy cosmic ray interactions*, (Tokyo: 1994), 711.
- Jerlov, N. J., 1976, *Marine Optics*, (Elsevier: Amsterdam).
- Jones, W. V., 1976, *Proceedings of the 1976 DUMAND Summer Workshop*, ed. A. Roberts, (Honolulu, Univ. of Hawaii), 591.
- Landau, L., and Pomeranchuk, I., 1953, *Dokl. Akad. Nauk SSSR* **92**, 535; 735.
- Levenberg, P., 1993, unpublished dissertation, Iowa State University Dept. of Physics.
- Lipari, P., 1993, *Astroparticle Physics*, **1**, 195.
- Matsuno, S., Babson, J., Learned, J. G., et al., 1989, *Nucl. Inst. Meth. A* **276**, 359.
- Migdal, A. B., 1956, *Physical Review* **103**, 1811.
- Miyake, S., 1973, *Proceedings of the 13th Int. Cosmic Ray Conf. (Denver: Univ. of Denver)*, vol 5, 3638.
- Mobley, C., *Light and Water*, 1994, (San Diego: Academic Press), 321.
- von Montigny, C., et al., 1996, *Astrophysical Journal* **440**, 525.
- Okada, A., 1994, *Astroparticle Physics* **2**, 393.
- Petzoldt, T. J., 1972, SIO ref. 72-78, Scripps Inst. of Ocean., La Jolla; condensed as ch. 12 in *Light in the Sea*, eds J. E. Tyler et al. 1977, 150-174.
- Price, P. B., et al, 1995, *Proceedings of the 24th International Cosmic Ray Conference, (Rome: IUPAP)* vol 1, 777.
- Protheroe, R. J., 1997, *Accretion Phenomena and Related Outflows, IAU Colloquium 163*, edited by D. T. Wickramasinghe, G. V. Bicknell, and L. Ferrario, (ASP Conference Series), vol 121.
- Reines, F., 1978, *Proceedings of the 1978 DUMAND Summer Workshop*, ed. A. Roberts, (Honolulu, Univ. of Hawaii), vol 2, 563.
- Resvanis, L. K., et al., 1995, *Proceedings of the 24th International Cosmic Ray Conference, (Rome: IUPAP)* vol 1, 1080.
- Rhode, W., et al., 1996, *Astroparticle Physics* **4**, 217

- Shifrin, K. S., 1983, *Physical Optics of Ocean Water*, transl. D. Oliver, AIP Transl. Ser., (AIP: New York) 1988; orig. publ. as *Vuedenei U Opticka Morya*, (Gidrometeoizdat: Leningrad), 1983.
- Smith, R. C., and Baker, K. S., 1981, *Appl. Optics* **20**, 177.
- Smith, R. C., and Tyler, J. E., 1976, in *Photochemical and Photobiological Reviews*, vol 1, K. C. Smith, ed., (Plenum: New York).
- Stecker, F. S., Salamon, M. H., 1996, *Space Science Reviews* **75**, 341 .
- Stecker, F. S., Done, C., Salamon, M. H., & Sommers, P., 1991, *Physical Review Letters* **66**, 2697, and *erratum*, 1992 in *Physical Review Letters* **69**, 2738.
- Szabo, A. P., and Protheroe, R. J., 1994, *Astroparticle Physics* **2**, 365.
- Wiebusch, C., 1995, unpublished doctoral dissertation, Aachen University, Aachen, Germany.